J. Fluid Mech. (2011), *vol.* 681, *pp.* 205–240.
doi:10.1017/jfm.2011.193

Instability of streaks in wall turbulence with adverse pressure gradient

MATTHIEU MARQUILLIE[1,2], UWE EHRENSTEIN[3]† AND JEAN-PHILIPPE LAVAL[1,2]

[1]CNRS, UMR 8107, F-59650 Villeneuve d'Ascq, France

[2]Université Lille Nord de France, F-59000 Lille, France

[3]IRPHÉ UMR 6594, Aix-Marseille Université, CNRS, F-13384 Marseille, France

(Received 7 May 2010; revised 6 January 2011; accepted 22 April 2011; first published online 2 June 2011)

A direct numerical simulation of a turbulent channel flow with a lower curved wall is performed at Reynolds number $Re_\tau \approx 600$. Low-speed streak structures are extracted from the turbulent flow field using methods known as *skeletonization* in image processing. Individual streaks in the wall-normal plane averaged in time and superimposed to the mean streamwise velocity profile are used as basic states for a linear stability analysis. Instability modes are computed at positions along the lower and upper wall and the instability onset is shown to coincide with the strong production peaks of turbulent kinetic energy near the maximum of pressure gradient on both the curved and the flat walls. The instability modes are spanwise-symmetric (varicose) for the adverse pressure gradient streak base flows with wall-normal inflection points, when the total average of the detected streaks is considered. The size and shape of the counter-rotating streamwise vortices associated with the instability modes are shown to be reminiscent of the coherent vortices emerging from the streak skeletons in the direct numerical simulation. Conditional averages of streaks have also been computed and the distance of the streak's centre from the wall is shown to be an essential parameter. For the upper-wall weak pressure gradient flow, spanwise-antisymmetric (sinuous) instability modes become unstable when sets of highest streaks are considered, whereas varicose modes dominate for the streaks closest to the wall.

Key words: instability, turbulent boundary layers

1. Introduction

Turbulent boundary layers with pressure gradient are present in many realistic internal and external aerodynamic flows (flow around turbine blades, aerofoils, to cite a few). Many different groups examined such flows with incipient separation or near separation. To understand flow which undergoes separation and subsequent turbulent reattachment is of prime importance to correctly predict the efficiency of many aerodynamic devices, such as lifting bodies or turbine blades. Such turbulent flows with *adverse pressure gradient* (APG) have however been regarded as being among

† Email address for correspondence: ehrenstein@irphe.univ-mrs.fr

the most challenging flow dynamics to predict using turbulence models according to Wilcox (1993). Flows influenced by a strong pressure gradient over a long streamwise distance are particularly difficult to model. The Reynolds stress equations, which are at the basis of the Reynolds-averaged Navier–Stokes equations, as well as the more accessible two equations models, include a number of terms that need to be modelled. The modelling is usually based on a scaling of the mean velocity profiles and turbulent quantities for a turbulent boundary layer in equilibrium. The mean velocity profile has been examined by a number of groups, with the object to recover collapsing profiles in different regions of the boundary layer. Most of these studies are conducted experimentally at large Reynolds numbers (see Skåre & Krogstad 1994; Bernard *et al.* 2003; Song & Eaton 2004). For a turbulent boundary layer with APG, several scalings have been proposed (Clauser 1954; Castillo & George 2001 and Aubertine & Eaton 2006) but none of them have been demonstrated to be valid for a large range of pressure gradients and Reynolds number. Taking benefit of the constant increase of numerical simulation capabilities, *direct numerical simulations* (DNS) of such flows with pressure gradient are now possible but restricted to small or moderate Reynolds numbers. The Reynolds number accessible by DNS has not significantly increased as compared to the first DNS of APG flows by Spalart & Watmuff (1993) or Na & Moin (1998). However, DNS has allowed to cover a large range of pressure gradients for attached or separated APG flows on flat walls or with various curvatures (see Skote & Henningson 2002; Lee & Sung 2008; Marquillie, Laval & Dolganov 2008; Lee & Sung 2009).

The effect of pressure gradient in turbulent boundary layer is not restricted to the difficulty in finding proper scaling for both the inner layer and for the outer region of the boundary layer. The APG also modifies significantly the distribution of Reynolds stresses as reported by many authors for different pressure gradients, with strong streamwise variation or nearly constant ones, as, for instance, in Skåre & Krogstad (1994). In the presence of APG, all the components of the Reynolds stress are affected and, independently from the first peak in the inner layer, a second peak appears and moves away from the wall. The intensity of the peak is variable and depends on the strength and the extent of the pressure gradient and consequently on the equilibrium state of the boundary layer. A comparison of several experiments and DNS of APG flows in various configurations and for a large range of Reynolds number was performed by Shah, Stanislas & Laval (2010). This study emphasizes the behaviour of the second peak in the streamwise component of the Reynolds stress. This second peak is reported to be located in the region between $y/\delta = 0.4$ and $y/\delta = 0.5$, except for the DNS of Spalart & Watmuff (1993) which is at a fairly low Reynolds number.

The underlying mechanism of the energy peak inherent in APG near-wall turbulence remains to be understood. It may be conjectured that the production of intense vortices associated with the peak is connected with the breakdown of more organized turbulent flow structures. A commonly admitted breakdown scenario which has been proposed for the late stages of transition processes to turbulence in wall-bounded flows is based on streak instabilities. The presence of elongated streaks gives rise to inflectional velocity profiles in the surrounding flow, exciting secondary instabilities which evolve into streamwise vortices, leading to a self-sustained process in shear flows (see Waleffe 1997). Streak instabilities have been studied in zero-pressure gradient shear flows, such as channel flows, confirming that the instability is of inflectional type and that the instability induces spanwise oscillations of the streak (Reddy *et al.* 1998; Elofsson, Kawakami & Alfredsson 1999). Sinuous (anti-symmetric) streak instability

modes have been shown in an experimental investigation by Mans, de Lange & van Steenhoven (2007) to be at the origin of natural breakdown in a flat-plate boundary layer with free-stream turbulence. Anti-symmetric perturbations are likely to be selected for inflectional streak base flow profiles in the spanwise direction, whereas wall-normal inflection points rather trigger varicose (symmetric) instability modes. Varicose modes have, for instance, been reported for streak distributions generated by nonlinear Görtler vortices in Hall & Horseman (1991).

Conducting an experiment in a low-turbulence wind tunnel, Asai, Manigawa & Nishioka (2002) provided evidence for secondary instabilities of streaks initiated by sinuous as well as varicose modes. It is shown in this latter work that hairpin-like structures with a pair of counter-rotating streamwise vortices result from the growth of the varicose mode. These findings, and in particular the streak breakdown associated with varicose modes, have been retrieved in the numerical study by Brandt (2007) who considered a single low-speed streak in a laminar boundary layer. Generating an isolated streak by blowing through a slot, reproducing an experimental investigation by Acarlar & Smith (1987), the varicose scenario of streak instability in a turbulent boundary layer has numerically been addressed in Skote, Haritonidis & Henningson (2002). Symmetric and anti-symmetric turbulent breakdown due to the interaction of streaks has been documented in Brandt & de Lange (2008). Further evidence of wall-turbulence generation through the instability and breakdown of low-speed streaks has been provided in Asai *et al.* (2007) for the zero-pressure gradient boundary layer. The mechanism leading to breakdown is shown to be consistent with the regeneration cycle of wall turbulence (Jiménez & Pinelli 1999). Focusing on the role of streak instability dynamics in wall-turbulence production, Schoppa & Hussain (2002) consider a representative steady low-speed streak superimposed to a turbulent mean velocity profile, corresponding to minimal channel turbulence (Jiménez & Moin 1991). The stability of this streak flow is analysed with the DNS-based approach which had previously been used for transition studies in free mixing layers (Schoppa, Hussain & Metcalfe 1995). It appears that only sufficiently strong streaks are unstable to sinuous modes, while streak transient growth is the dominant vortex generation mechanism for the streak model considered in Schoppa & Hussain (2002).

Streak instability in APG turbulent boundary layers has found less attention. Here, we aim at assessing a possible link between the above-mentioned turbulent kinetic energy peak observed in our simulation data and a streak instability. For this purpose, in a first step, a technique known as *skeletonization* in image processing (Palágyi & Kuba 1999) is used to isolate from the turbulent database averaged low-speed streak structures. Superimposing the mean velocity profile, a stability analysis of the streak base flow, varying in both the wall-normal and spanwise coordinate, is performed by solving the corresponding eigenvalue problem, using a locally parallel flow assumption along the wall of the divergent–convergent channel. The outline of the paper is as follows: in § 2, the DNS-procedure is described and some details of the turbulent APG flow are provided. The streak detection method is briefly explained in § 3. First, the method is applied in § 4 to a turbulent zero-pressure gradient channel flow and the stability results for the resulting streak base flows are discussed. The characteristics of the low-speed streak for the non-parallel APG flow are investigated in § 5 and the stability results for streak base flows along the upper wall and the lower curved wall of the channel are provided. In § 6, the connection between the instability prediction and the coherent structure dynamics in the simulation data for the APG wall turbulence is discussed and some conclusions are drawn.

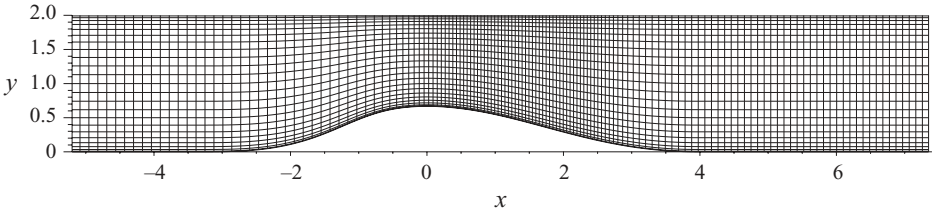

FIGURE 1. Computing grid of the DNS in the (x, y) plane (every 16 meshes are plotted in each direction). The flow is coming from the left.

2. Direct numerical simulation

2.1. *The DNS procedure*

The algorithm used for solving the incompressible Navier–Stokes system is similar to the one described in Marquillie *et al.* (2008). To take into account the complex geometry of the physical domain (see figure 1), the partial differential operators are transformed using the mapping that has the property of following a profile at the lower wall with a flat surface at the upper wall. Applying this mapping to the momentum and divergence equations, the modified system in the computational coordinates has to be solved in the transformed Cartesian geometry.

The three-dimensional Navier–Stokes equations are discretized using fourth- and eighth-order centred finite differences in the streamwise x-direction. A pseudo-spectral Chebyshev collocation method is used in the wall-normal y-direction. The spanwise z-direction is assumed periodic and is discretized using a spectral Fourier expansion, the nonlinear coupling terms being computed using a conventional de-aliasing technique (3/2-rule). The resulting 2D Poisson equations are solved in parallel using MPI library. Implicit second-order backward Euler differencing is used for time integration, the Cartesian part of the diffusion term is taken implicitly whereas the nonlinear and metric terms (due to the mapping) are evaluated using an explicit second-order Adams–Bashforth scheme. In order to ensure a divergence-free velocity field, a fractional-step method has been adapted to the present formulation of the Navier–Stokes system with coordinate transformation.

The objective of the DNS is to work out a database of a turbulent flow with adverse pressure gradient at the highest accessible Reynolds number and with a geometry comparable to the experiment which was carried on in the LML wind tunnel (Bernard *et al.* 2003). A channel flow configuration was chosen instead of two separated boundary layers because channel flow inlet conditions are much easier to generate. The reason is the difficulty in defining a *a priori* simulation which leads to two different boundary layers with statistics comparable to the experiment. Therefore, the inlet conditions are generated by precursor DNS of flat channel flows at the equivalent Reynolds numbers. The simulation domain for the DNS with APG is 4π in the streamwise x direction, 2 in the normal y direction and π in the spanwise z-direction. The Reynolds number based on the inlet friction velocity ($u_\tau^\circ = 0.0494$) and half the channel height h is $Re_\tau = 617$. The spatial resolutions are $2304 \times 385 \times 576$ in the streamwise, normal and spanwise direction, respectively. The grid is stretched in the streamwise direction (see figure 1) in the region of strong pressure gradient. The computation has been performed on 64 vector processors on the NEC SX8 at the High Performance Computing Center of Stuttgart (HLRS), with a sustained 640 Gflops performance. The simulation was integrated over 50 convective times (based

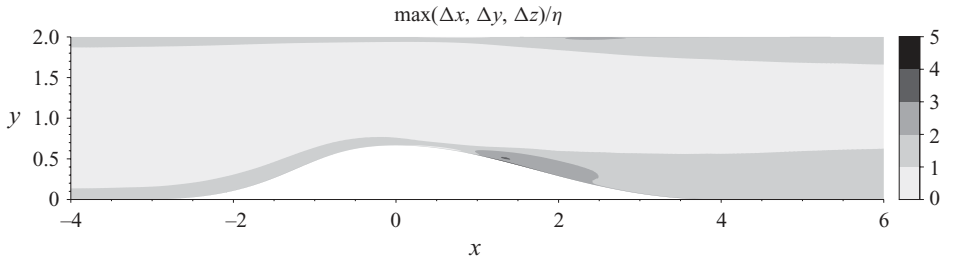

FIGURE 2. Spatial resolution of the DNS as compared to the Kolmogorov scale $\eta = \nu^{3/4}/\epsilon^{1/4}$. Δx, Δy, Δz are the mesh sizes in streamwise, normal and spanwise direction, respectively.

on half the channel height and the maximum velocity at the inlet) ensuring statistical convergence and the statistics were computed over 972 velocity and pressure fields equally distributed in time.

The ratio of the Kolmogorov scale $\eta = (\nu^3/\epsilon)^{1/4}$ with respect to the maximum mesh size is shown in figure 2. The maximum of this ratio is lower than 2 almost everywhere in the simulation domain and it takes values of 3.02 in the diverging part and up to 5 very close to the wall (not visible in the figure). However, in order to evaluate the spatial resolution of the near-wall region, the mesh sizes in wall units (Δx^+, Δy^+, Δz^+) are more relevant. Their maximum values at the inlet are $\Delta x^+ = 5.1$, $\Delta y^+_{min} = 0.02$ and $\Delta z^+ = 3.4$. The global maximum values are reached in the converging part of the channel with $\Delta x^+ = 10.7$, $\Delta y^+_{min} = 0.03$ and $\Delta z^+ = 7.4$.

2.2. *Characterization of the flow*

The pressure coefficient of the DNS is compared with the experiment of Bernard *et al.* (2003) (see figure 3). The observed differences between the experiment and the DNS are expected. Indeed, the inlet conditions are different and the Reynolds number in the experiment is more than one order of magnitude higher than in the numerical simulation. In order to characterize the pressure gradient, the non-dimensional quantity $P^+ = \nu(\mathrm{d}P/\mathrm{d}x)/(\rho u_\tau^3)$ was preferred over the Clauser parameter $\beta = (\delta^*/\tau_w)\,\mathrm{d}P/\mathrm{d}x$. Indeed, channel flow inlet conditions are used and the boundary-layer displacement thickness δ^* cannot be defined accurately for the whole flow. The streamwise evolution of P^+ is given in figure 3 at the two walls. At the lower wall, the sign of the pressure gradient changes at $x = -0.2$ and P^+ increases very sharply near $x = 0.2$. The value of P^+ is not shown for $0.5 < x < 1.5$ which corresponds to the recirculation region. The curve exhibits a small plateau ($P^+ \simeq 0.3$) in the recovery region for $1.8 < x < 2.6$ and monotonically decrease to zero by the end of the bump. The evolution of the pressure gradient at the flat upper wall is smoother: P^+ becomes positive near $x = 0.2$ and rises up to $P^+ = 0.8$ at $x = 1.7$. The pressure gradient grows more progressively than for the lower wall and the maximum increase is shifted downstream near $x = 1.3$. The position of the maximum growth of P^+ is important and will be related to the instability analysis in § 5.2.

The friction coefficients $C_f = \tau_w/(\frac{1}{2}\rho U^2_{max})$ are compared for the two walls in figure 4. The graph indicates that the flow slightly separates at the lower wall (contrary to the experiment at much higher Reynolds number) but not at the upper wall. The minimum friction velocity as well as the minimum of pressure coefficient at the upper wall are moved forward by $\delta x \simeq 0.5$ as compared to the lower wall. The lower intensity of the pressure gradient as well as the absence of curvature at the upper wall lead to a positive minimum friction velocity $C_f = 1.55 \times 10^{-3}$. The detachment

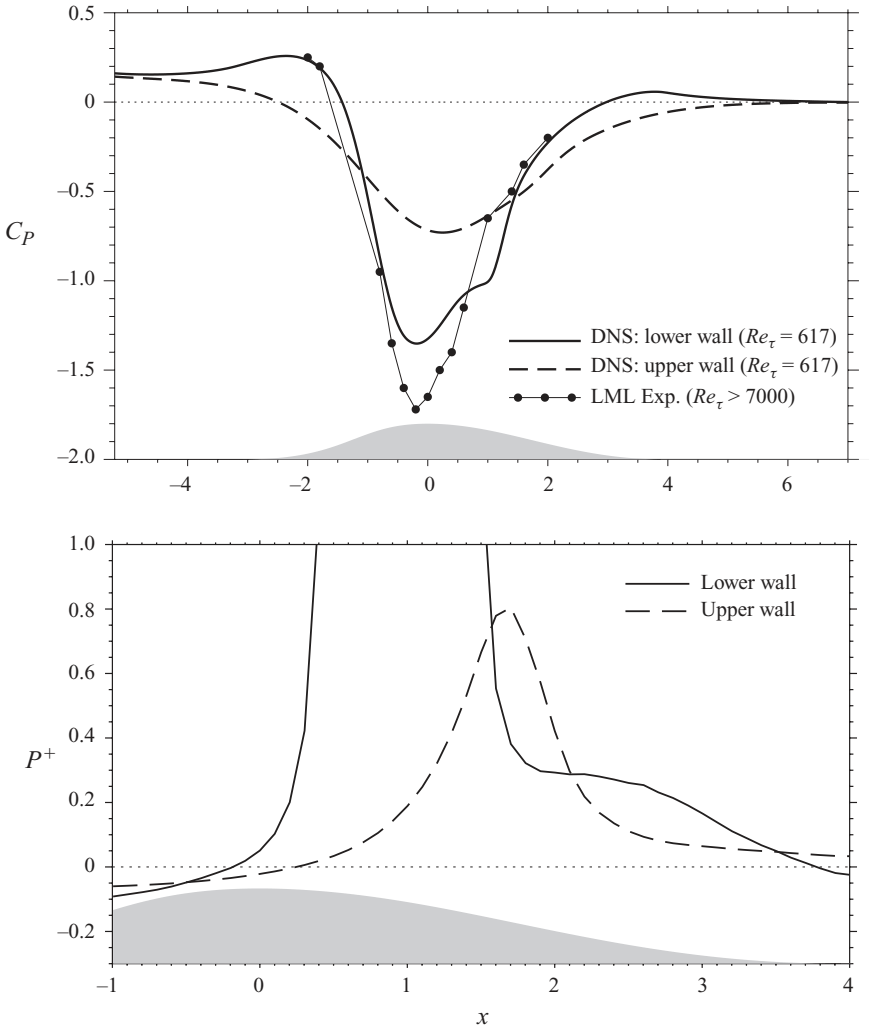

FIGURE 3. Pressure coefficient $C_p = (P - P_o)/((1/2)\rho U_{max}^2)$ and dimensionless pressure gradient parameter $P^+ = (\nu/u_\tau^3)(\partial P/\partial x)$. The pressure coefficient of the experiment (at the lower wall) of Bernard *et al.* (2003) is given as a reference, and the Re_τ of the experiment is roughly estimated from the boundary-layer thickness in front of the geometry.

region can be defined by using the probability density function of reverse flow γ_u. Simpson (1981) defined four different states of a separating turbulent boundary layer: incident detachment for $\gamma_u > 0.01$, intermittent transitory detachment for $\gamma_u > 0.2$ and transitory detachment for $\gamma_u > 0.5$. The detachment occurs when the time-averaged wall shearing stress is zero. The result of γ_u is shown in figure 4 for the lower wall. In this case, the region of transitory detachment and detachment almost coincide and is restricted between $x = 0.5$ and $x = 1.4$. Using these definitions, the maximum thickness of the recirculation zone is approximately 0.03 which corresponds to less than 20 wall units based on inlet quantities. The probability of reverse flow is not shown at the upper wall as the maximum value is lower than 0.33 and the region with $\gamma_u > 0.01$ is much thinner than for the lower wall.

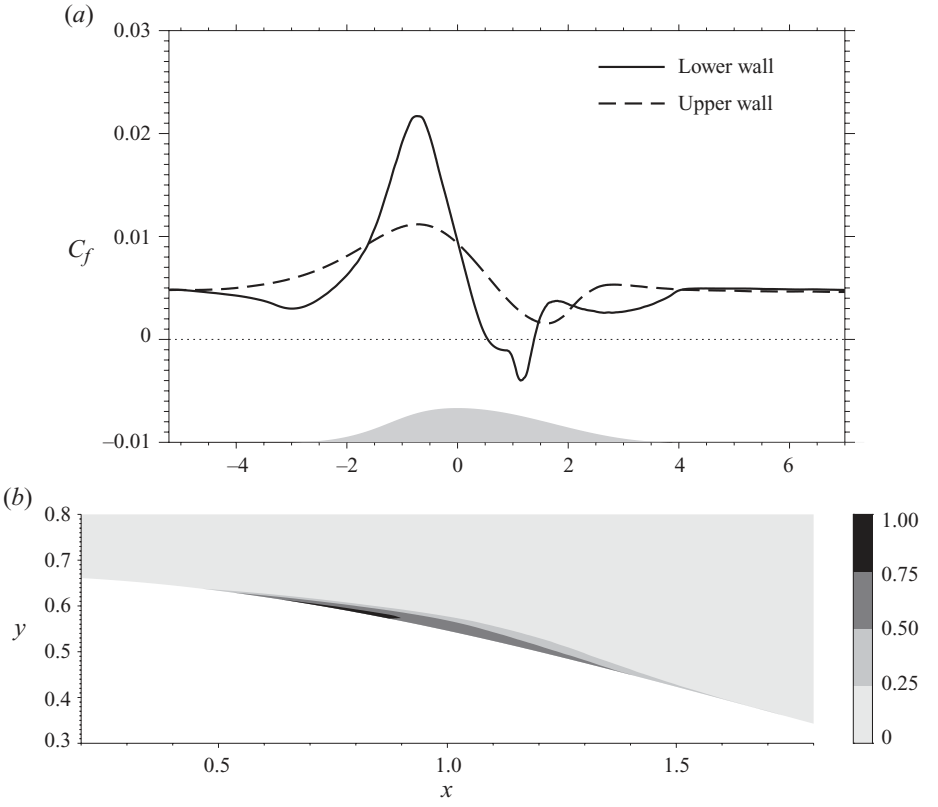

FIGURE 4. Skin friction coefficient $C_f = \tau_w/((1/2)\rho U_{max}^2)$ (*a*) and probability density function of reverse flow γ_u (*b*) at the lower wall. A very thin region of reverse flow is present at the upper wall (not shown) but the maximum probability of reverse flow is lower than 0.33.

As we are dealing with channel flow inlet instead of real turbulent boundary layer, the size of the boundary layers cannot be defined accurately. However, it is of interest to have a rough estimation in order to be able to scale and to localize statistical phenomena and coherent structures inside the boundary layer. The pressure gradient at the upper wall is obviously too low to recreate a well-defined boundary layer from the channel flow profile and the characteristics of the boundary layer have been estimated only at the lower wall. The definition of the boundary-layer thickness δ was adapted to extract from the channel profile the upper bound of the boundary layer formed near the wall by using the following criteria: $U(y) > 0.8\ U_{max}$ and $\mathrm{d}U/\mathrm{d}y(y) < 0.25\ U_{max}/h$. The streamwise range where these criteria are satisfied is shown in figure 5. The boundary-layer thickness is seen to be minimum at the position of the maximum of friction coefficient ($\delta = 0.042$ near $x = -0.7$) and increases up to $\delta = 0.1$ at $x = 0.8$. It is interesting to note that the value $\delta = 0.06$ at the summit of the bump corresponds to approximately 40 wall units based on u_τ° at the inlet. The momentum thickness (θ) and the shape factor have also been computed. Due to the effect of pressure gradient, the shape factor rises from $H \simeq 2$ to $H > 4.5$ near the centre of the thin separation region. The increase is slow and nearly linear up to $x = 0.1$ and the slope suddenly increases near $x = 0.22$. This position will be of importance for the instability results to be discussed.

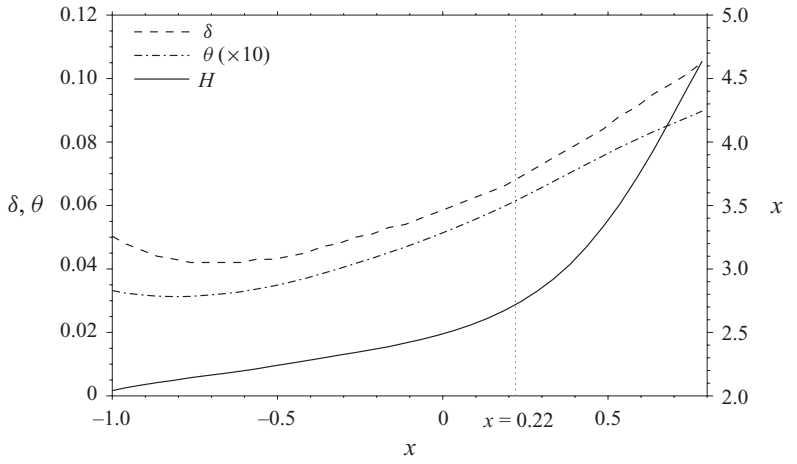

FIGURE 5. Statistics of the turbulent boundary layer above the lower bump. The boundary layer thickness (δ), defined such that $U(y) > 0.8\, U_{max}$ and $\mathrm{d}U/\mathrm{d}y(y) < 0.25 U_{max}/h$, momentum thickness ($\theta$) and shape factor ($H$) are given for a limited range of streamwise positions where they can be defined with a fair accuracy.

FIGURE 6. Iso-value of the Q–criterion ($Q = \frac{1}{2}[|\boldsymbol{\Omega}|^2 - |\boldsymbol{S}|^2]$ with $\boldsymbol{S} = \frac{1}{2}[\nabla u + (\nabla u)^{\mathrm{T}}]$ and $\boldsymbol{\Omega} = \frac{1}{2}[\nabla u - (\nabla u)^{\mathrm{T}}]$) for the whole simulation domain.

The objective of the present study is not to give a complete statistical description of the DNS near-wall turbulence. A brief overview of the distribution of the Reynolds stresses and the budget of the turbulent kinetic energy is provided in Laval & Marquillie (2009) and a more complete analysis was done by Marquillie *et al.* (2008) for a DNS of the same flow and the same geometry but at a lower Reynolds number ($Re_\tau = 395$ instead of $Re_\tau = 617$). These two analyses stress a strong production peak of turbulent kinetic energy near the maximum of pressure gradient on both the flat and the curved walls. As already observed by many authors, the three normal components of the Reynolds stresses are enhanced. This strong modification of the Reynolds stresses reveals the production of intense coherent vortices muddled by complex interactions. Iso-values of the second invariant Q of the velocity gradient tensor shown in figure 6 gives evidence of these strong coherent vortices. These structures suddenly emerge at x positions which are in the range of the strong pressure gradient variations shown in figure 3. A detailed analysis of these vortices shows that their intensity defined by their average vorticity is much larger than the average intensity in a zero-pressure-gradient turbulent boundary layer or a flat turbulent channel flow.

3. Streaks detections

Streaks are known to be a fundamental element in turbulent boundary-layer flows. Numerous studies have been devoted to extract key features and statistical characteristics of the streaks in order to better understand their role in wall-bounded flows (see Lin *et al.* 2008 for a recent review). Most of the previous studies have used experimental data for zero-pressure-gradient flows. Here, the objective is to analyse the effect of the pressure gradient on the streaks characteristics. For this purpose, a detection procedure has been developed to extract the centreline of the streamwise low-speed streaks from the three-dimensional instantaneous velocity fields. The streaks detection procedure is mainly based on a "skeletonization" algorithm. The idea of these algorithms is to find a curve (a skeleton) representative of a shape in space. This skeleton is defined to be equidistant to the shape's boundary and is responsible for maintaining its topology. Skeletons are used in a wide range of applications in computer vision, image analysis and digital image processing. Medical image analysis, pattern recognition and fingerprint recognition being some well-known applications of these techniques. The detection process consists of the following main steps: thresholding of the input data, topological correction of the binary image and centreline extraction by thinning and pruning. Examples of similar procedures applied to elongated structures in medical image processing can be found, for instance, in Palágyi *et al.* (2006).

The first step is to identify the structure objects in the velocity field. We use the same detection function used by Lin *et al.* (2008) for streaks detection from two-dimensional instantaneous velocity fields obtained from PIV measurements. The three-dimensional binary image of streaks is obtained by applying a threshold directly to the normalized streamwise velocity fluctuation field. The resulting binary field, interpolated on a regular grid for application of the skeletonization algorithms, is composed of "1" voxel for the low-speed streaks and "0" voxel otherwise (a voxel is the equivalent in 3D of a pixel which represents 2D image data). A top view of the thresholding results is shown in figure 7(*a*) for a small region of the lower wall.

Thresholding may produce imperfect results leading to segmented objects having small holes and protrusions on the object boundary. These small imperfections can alter the centreline detection by creating undesirable small lines connecting the main centreline of the streaks to the boundary. Classical mathematical morphological operators (see Gonzales & Woods 2008) are commonly used as a pre-processing step to improve the binary field before applying the skeleton detection. As a first step, holes are filled by applying morphological closing operations (a dilatation followed by an erosion). Then, a morphological opening (an erosion followed by a dilatation) is employed to remove the protrusions and the surface layers as a result of the closing operation. Dilatation and erosion operations are parameterized by a 3D structuring element which has been empirically determined in order to preserve, in a conservative way, the shape of the binary objects. An example of this topological correction after the thresholding can be seen in figure 7(*b*).

Several algorithms have been developed to extract the skeleton of a binary object (see Cornea, Silver & Min 2007 for an extensive review). Thinning is a frequently used method to extract centrelines in a topology-preserving way. This algorithm consists of deleting step by step border points of a binary object that satisfy topological and geometric constraints, until only the centreline remains. The curve–thinning algorithm chosen here (Palágyi & Kuba 1999) has the additional property of producing directly one-voxel-wide centrelines. The thinning algorithm applied to the corrected binary image is shown in figure 7(*b*). The centreline of the elongated streak is clearly identified

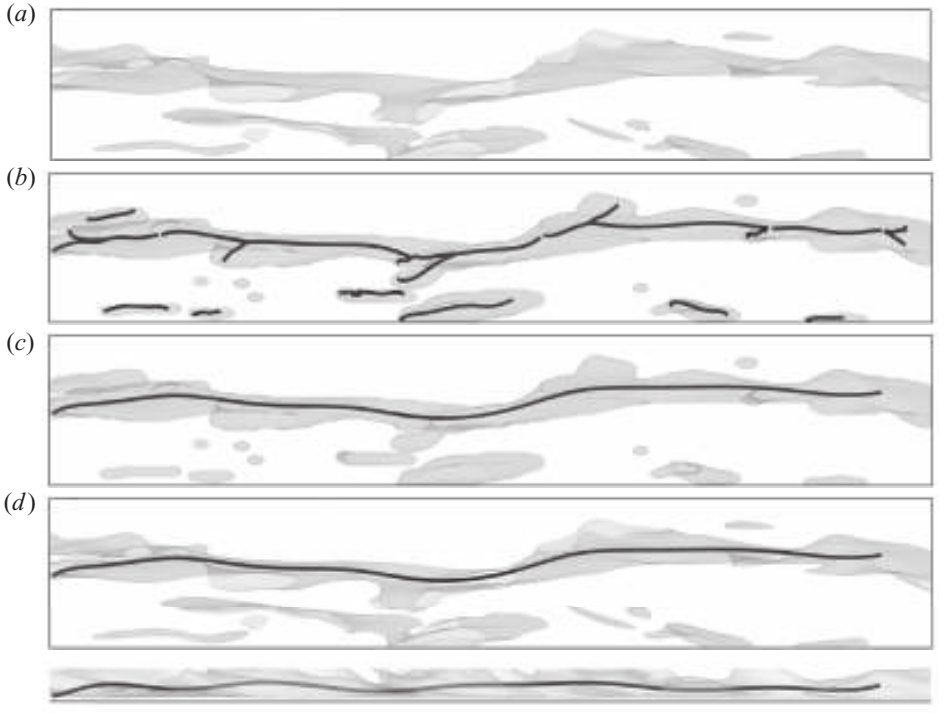

FIGURE 7. Example of the streaks detection procedure on a small region: (*a*) thresholding; (*b*) topological correction and thinning; (*c*) pruning; (*d*) streak centreline on original thresholding (top and side view).

by the algorithm; however, small additional branches coming from the remaining protrusions on the surface of the tubular object can be seen. Also, skeletons appear in small structures that cannot be identified as streaks.

In order to retain only the main centreline of the streaks, a cleaning procedure, classically called pruning, is performed. The first step consists of removing the small structures using a suitable threshold based on the total number of points in the skeleton. The next step consists of removing side branches of the remaining skeletons for which we applied a standard pruning approach called morphological pruning. This procedure involves two phases. First, the branches are labelled by identifying special points of the skeleton, such as end-points and branch-points. Then, the side branches shorter than a predefined threshold are removed (see Gonzales & Woods 2008 for further details). The final result of the full detection procedure, after the pruning, is shown, both on the corrected binary image (see figure 7*c*) and on the original image after thresholding (see figure 7*d*).

4. Zero-pressure-gradient turbulent channel flow

4.1. *Streaks averaging procedure*

The procedure described in the last section is able to detect all individual low-speed streaks (called simply *streaks* in the following) of a near-wall turbulent flow. The detection is based on a thresholding of the fluctuating velocity and as can be

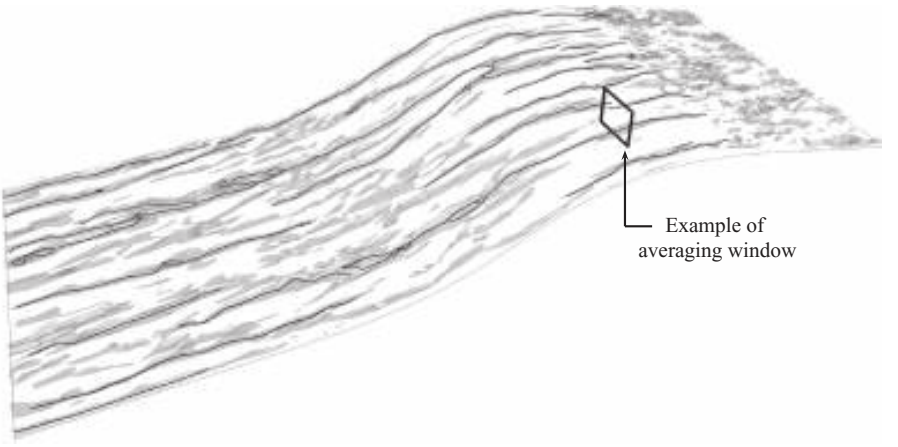

FIGURE 8. Results of the detection of the low-speed streaks at the lower wall in the converging part of the domain. The skeletons are indicated with dark tubes down to $x = 1.3$ as the 3D visualization indicates that the streaks are totally destroyed further downstream.

seen in figure 8, despite the image processing treatments, the detected streaks are fairly complex (with some multiple branches/skeletons still visible) and only those which are sufficiently long and representative of well-defined streaks were retained for the statistics. In the following, (x_c, y_c, z_c) will denote the coordinates of the points detected as centrelines of streaks. The objective of the present study is not to accurately characterize the full range of streaks but rather to define a realistic streak on average. For this purpose, a conditional average of the streamwise velocity fluctuations in the normal plane (y, z) in the vicinity of the detected streaks has been computed. The average is defined as

$$\langle u' \rangle_x (y, z) = \sum_t \sum_{x_c = x, z_c} u'(x, y, z - z_c, t) G(y, z - z_c), \tag{4.1}$$

where G is an averaging window of fixed size (an example is shown in figure 8) centred at the z_c spanwise location of each streak skeleton. The streamwise velocity fluctuation values within all these averaging windows (in the spanwise direction and time) are collected and an average streak $\langle u' \rangle_x (y, z)$ is recovered for each streamwise location x. The width of the window has been chosen sufficiently large in each case to recover the low-speed streak and the two adjacent high-speed streaks.

4.2. *Characterization of average low-speed streaks in flat-channel flow*

The detection procedure has first been applied to the results of turbulent channel flows from del Álamo & Jiménez (2003) and del Álamo *et al.* (2004) at three different Reynolds numbers ($Re_\tau = 180$, $Re_\tau = 550$ and $Re_\tau = 950$). For $Re_\tau = 180$, the statistics were performed with 100 velocity fields of size $12\pi \times 2 \times 4\pi$. For the larger Reynolds numbers, 10 velocity fields of size $8\pi \times 2 \times 4\pi$ and $8\pi \times 2 \times 3\pi$, respectively, proved sufficient for the statistics. As the spacing between streaks scales in wall units, the number of streaks in each simulation box increases as Re_τ^2 leading to approximately the same order of streaks samples for the three cases. The value of the threshold used to extract the streak was set to $u' = C\, u_m^{rms}$ as recommended by Lin *et al.* (2008) (u_m^{rms} being the maximum over y of u'^{rms} at each streamwise position). The constant C was chosen to detect most representative streaks and to avoid as much as possible small (or non-physical) ones in the outcome of the procedure. Here, the only output

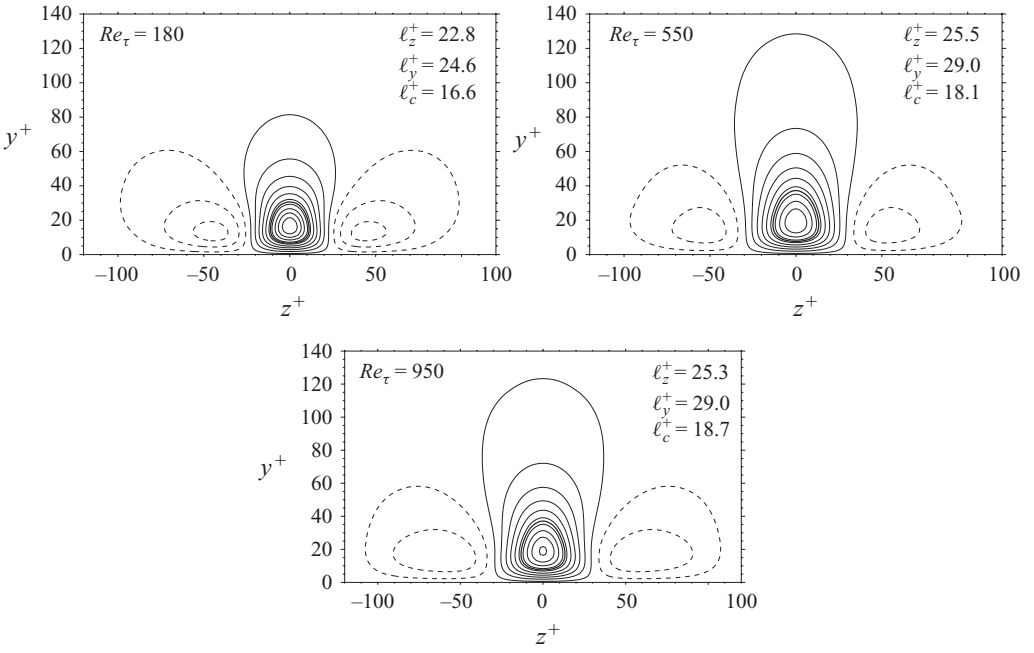

FIGURE 9. Averaged streaks $\langle u' \rangle$ for the channel flows (del Álamo *et al.* 2004) at three Reynolds numbers ($Re_\tau = 180$, $Re_\tau = 550$ and $Re_\tau = 950$). The streaks are visualized with negative (continuous lines) and positive (dashed lines) iso-contours (with increment $0.15\, u_m^{rms}$) of conditional average of the fluctuating streamwise velocity in the vicinity of low-speed streaks detected using the procedure described in § 3. The iso-contour corresponding to the detection threshold ($u' = -0.9\, u_m^{rms}$) is plotted with a continuous thick line.

which will be used is the spanwise location of the streak's centre z_c. The value of the constant C is therefore much less critical than it would be for the full characterization of each individual streak (see Lin *et al.* 2008). For the flow cases at the different Reynolds numbers, the same threshold of streamwise velocity $u' = -0.9\, u_m^{rms}$ is used for the detection procedure of the individual streaks. It has been checked that the resulting locations of the streak's centre (x_c, y_c, z_c) coincide or differ only by one mesh size from the local minimum of the fluctuation streamwise velocity.

For the parallel flat channel, the average low-speed streaks $\langle u' \rangle_x(y, z)$ at the streamwise positions x have been averaged also over all x and the results $\langle u' \rangle(y, z)$ at the three Reynolds numbers are shown in figure 9. The thick contour defines the typical size of the streaks and corresponds to the isoline equal to the threshold of streamwise velocity used in the detection procedure. The width l_z and height l_y of the averaged streak as well as the position of its centre l_c (defined by the minimum of the averaged streamwise velocity) are indicated for each Reynolds number. The shapes and sizes are almost identical in wall units for the two largest Reynolds numbers but slightly differ for $Re_\tau = 180$. This analysis reveals the Reynolds number dependency at low Reynolds numbers. The average width ($l_z^+ \simeq 25$) and average height ($l_y^+ \simeq 29$) of streaks for the two largest Reynolds numbers are in good agreement with predictions of many authors including Lin *et al.* (2008) from experimental results in a turbulent boundary layer at a much higher Reynolds number.

In order to qualify the variety of streaks, the probability density function of their intensity is investigated. Several parameters have been already introduced to quantify

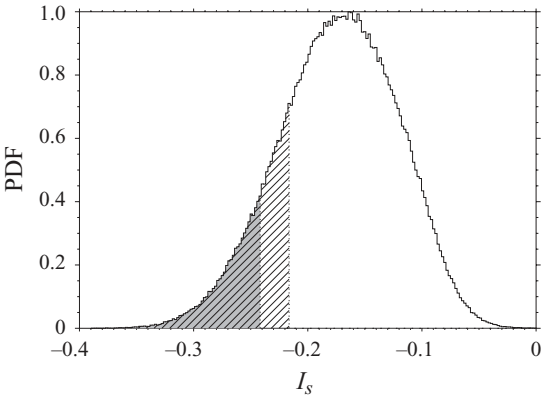

FIGURE 10. Probability density function of the intensity of streaks detected for the channel flow at $Re_\tau = 550$. The intensity I_s is defined as the normalized average fluctuating streamwise velocity around the streaks in a normal plane (see (4.2)). The probability corresponding to the 20% and 10% stronger streaks are indicated with the hatching and grey shading, respectively.

the streaks intensity. In Andersson *et al.* (2001) the so-called A-criterion measures the normalized streamwise velocity differences between the extrema of the low-speed streaks and their adjacent high-speed streaks. A more elaborated parameter was introduced by Schoppa & Hussain (2002). This other criterion θ is defined as the maximum angle of the isovalues of the streamwise velocity in the neighbourhood of a low-speed streak at a constant characteristic streak centre height. These two criteria are not direct measurements of the intensity of the low-speed streaks. According to the definitions, the parameter A, as well as θ, also depend on the intensity of the associated high-speed streaks. Furthermore, the parameter θ depends on the wall distance of the centre of the low-speed streak in a non-trivial way. In order to quantify more precisely the intensity of the single low-speed streaks, a new parameter I_s is defined as the normalized averaged streamwise fluctuating velocity in the vicinity of the low-speed streak centre in the (y, z) plane with

$$I_s = \frac{1}{l_y l_z} \frac{1}{u_{max}} \int_{-l_z/2}^{+l_z/2} \int_{-l_y/2}^{+l_y/2} u'(y - l_c, z - z_c)\, \mathrm{d}y\, \mathrm{d}z, \tag{4.2}$$

u_{max} being the maximum value of the mean streamwise velocity profile. The intensity I_s is computed for the channel flow at $Re_\tau = 550$ at each streamwise position x of each branch of detected streaks, using statistics of the average quantities (l_y, l_z and l_c) computed in a previous step. The probability density function computed on all streamwise locations is shown in figure 10 for $Re_\tau = 550$. The averaged intensity is -0.17 and the distribution is close to a Gaussian. The intensities corresponding to the 20% and 10% stronger streaks are also indicated as their characteristics will be discussed in a following section on stability analyses. In order to compare the three criteria of intensity, the average of the 10% strongest low-speed streaks are computed using the three definitions of intensity (I_s, A and θ). The result is shown in figure 11. The average formed with the 10% strongest streak using the criterion I_s exhibits the strongest streak core. As expected, the average with the 10% largest values of A produces streaks with strong adjacent high-speed streaks. In the present identification procedure of streaks, the streak's centre is determined and the θ-criterion was evaluated at the height corresponding precisely to each individual

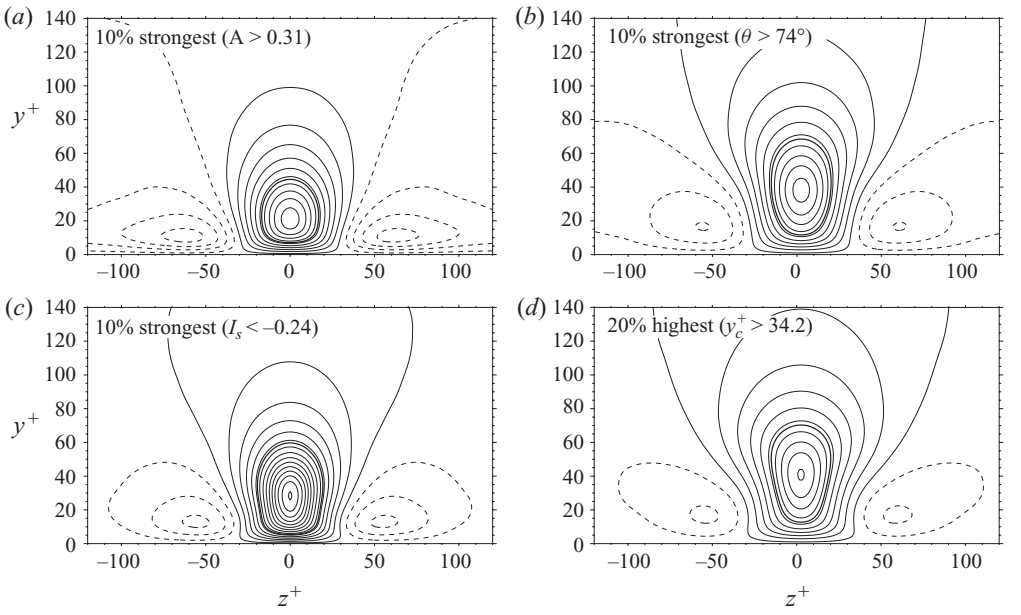

FIGURE 11. Conditionally averaged streaks ($\langle u' \rangle$), visualized with negative (continuous lines) and positive (dashed lines) iso-contours (increment 0.15 u_m^{rms}), for the turbulent channel flow at $Re_\tau = 550$. The average of the 10% strongest streaks according to the A-criterion (a), the θ-criterion (b) and the intensity I_s-criterion (c). d: average of the 20% highest streaks according to the distance of the streak's centre y_c^+ from the wall.

low-speed streak centre y_c. Note that in Schoppa & Hussain (2002), θ is evaluated at several constant wall distances ranging from 10 to 30 wall units. The average low-speed streak evaluated with the 10% largest values of θ proved to be less intense and it exhibits a centre at some higher distance from the wall than the averaged streak using the A criterion (see figure 11). This comparison confirms that θ can be seen as a measure of both the intensity and the wall distance of the streaks.

Most of the studies on streaks instability focused on the streaks intensity. However, the wall-normal position of the streaks with respect to the normal gradient of mean streamwise velocity is also expected to play a significant role in the instability, as it strongly affects the curvature of the mean velocity isolines. In the following section, instability analyses will be conducted for the averages of five different subsets of low-speed streaks, defined by the height of their centre y_c by bands of 20%. The streak base flows for the 20% highest and the 10% strongest streaks are compared in figure 11. The strength of the averaged 20% highest low-speed streaks is seen to be weaker than that of the averaged 10% strongest streaks defined with I_s but it is comparable to the average using the A and θ criteria. The main difference is the lower intensity of the associated high-speed streaks. The stability of the four conditionally averaged streaks of figure 11 will be investigated in the following section.

4.3. *Stability equations and numerical procedure*

The linear stability of streaks has found a lot of attention since the pioneering work of Waleffe (1997) who identified streak instability as a key element for self-sustained processes in near-wall regions of transitional and turbulent shear flows. Zero-pressure-gradient boundary layer streaks have, for instance, been considered in Brandt & Henningson (2002) and Hoepffner, Brandt & Henningson (2005), for streaks

arising from the so-called lift-up effect associated with the presence of streamwise vortices as optimal disturbances of unstable shear flows (Schmid & Henningson 2001). For turbulent channel flow, Schoppa & Hussain (2002) consider representative streak structures for linear stability analyses. Before we address, in the next section, the instability of streaks in the presence of adverse pressure gradients, which has found less attention up to now, we first provide some results for the turbulent channel flow.

Superimposing averaged streaks and the mean velocity profile, one recovers for the parallel channel flow a streamwise velocity $\bar{U}(y, z)$, called in the following as *streak base flow*, which is considered as the basic state for a modal instability analysis. In this parallel setting, the velocity and pressure perturbations are

$$\boldsymbol{u}(x, y, z, t) = (\hat{u}(y, z), \hat{v}(y, z), \hat{w}(y, z))\, \mathrm{e}^{\mathrm{i}(\alpha x - \omega t)}, \quad p = \hat{p}(y, z)\, \mathrm{e}^{\mathrm{i}(\alpha x - \omega t)}, \tag{4.3}$$

the perturbation being unstable if the imaginary part ω_i of the complex temporal eigenvalue $\omega = \omega_r + \omega_i$ is positive. Linearizing the Navier–Stokes at the base state $(\bar{U}(y, z), 0, 0)$, the perturbation modes are solution of

$$-\mathrm{i}\omega\hat{u} = -\bar{U}\mathrm{i}\alpha\hat{u} - \hat{v}\frac{\partial\bar{U}}{\partial y} - \hat{w}\frac{\partial\bar{U}}{\partial z} - \mathrm{i}\alpha\hat{p} + \frac{1}{Re}\left(\frac{\partial^2\hat{u}}{\partial y^2} + \frac{\partial^2\hat{u}}{\partial z^2} - \alpha^2\hat{u}\right), \tag{4.4}$$

$$-\mathrm{i}\omega\hat{v} = -\bar{U}\mathrm{i}\alpha\hat{v} - \frac{\partial\hat{p}}{\partial y} + \frac{1}{Re}\left(\frac{\partial^2\hat{v}}{\partial y^2} + \frac{\partial^2\hat{v}}{\partial z^2} - \alpha^2\hat{v}\right), \tag{4.5}$$

$$-\mathrm{i}\omega\hat{w} = -\bar{U}\mathrm{i}\alpha\hat{w} - \frac{\partial\hat{p}}{\partial z} + \frac{1}{Re}\left(\frac{\partial^2\hat{w}}{\partial y^2} + \frac{\partial^2\hat{w}}{\partial z^2} - \alpha^2\hat{w}\right), \tag{4.6}$$

$$0 = \mathrm{i}\alpha\hat{u} + \frac{\partial\hat{v}}{\partial y} + \frac{\partial\hat{w}}{\partial z}. \tag{4.7}$$

Note that the stability equations are made dimensionless using half the channel height at inflow as reference length. Natural symmetries arise in the mode structure with respect to the centre $z = 0$ of the spanwise box. According to the commonly used classification (see, for instance, Asai *et al.* 2002), varicose modes are such that the streamwise perturbation velocity component $\hat{u}(y, z)$ is symmetric, i.e. $\hat{u}(y, -z) = \hat{u}(y, z)$, whereas $\hat{u}(y, z)$ for sinuous modes is anti-symmetric with $\hat{u}(y, -z) = -\hat{u}(y, z)$. The Chebyshev-collocation discretization is used in both the wall-normal y direction and the spanwise z coordinate. The wall corresponds to $y = 0$, where the no-slip condition for the perturbation flow velocity is imposed. In all the stability computations, the wall-normal coordinate extends to a distance $y_{max} = 1$ from the wall, where the perturbation velocity is prescribed to be zero.

The stability computations have been performed for the turbulent channel flow with $Re_\tau = 550$, that is in wall coordinates $y^+_{max} = 550$, which indeed is far from the turbulent wall boundary layer. In the spanwise direction $-a \leqslant z \leqslant a$, periodic boundary conditions are applied for the perturbation flow velocity and pressure, i.e.

$$[\widehat{\boldsymbol{u}}, \hat{p}](y, -a) = [\widehat{\boldsymbol{u}}, \hat{p}](y, a), \quad \left[\frac{\partial\widehat{\boldsymbol{u}}}{\partial z}, \frac{\partial\hat{p}}{\partial z}\right](y, -a) = \left[\frac{\partial\widehat{\boldsymbol{u}}}{\partial z}, \frac{\partial\hat{p}}{\partial z}\right](y, a). \tag{4.8}$$

The incompressibility condition is applied everywhere in the domain $0 \leqslant y \leqslant 1, -a < z < a$, and the system once discretized gives rise to the generalized eigenvalue problem

$$-i\omega\boldsymbol{B}\boldsymbol{v} = \boldsymbol{A}\boldsymbol{v}. \tag{4.9}$$

Here, the vector $\boldsymbol{v}$ contains the disturbance flow velocity and pressure. The operator $\boldsymbol{B}$ corresponds to the projection onto the discretized velocity components and $\boldsymbol{A}$

corresponds to the discretized right-hand side of system (4.4)–(4.7). The near-wall gradients have to be solved and in the forthcoming analysis $N_y = 300$ collocation points have been considered in the wall-normal direction, which proved to be sufficient for convergence of the stability results. Note that owing to the accumulation of the Chebyshev collocation points near the wall, seven discretization points are in the region below one reference wall unit $y^+ = 1$ and the distance up to $y^+ = 100$ (which corresponds to $y \approx 0.18$) contains 80 points. Up to $N_z = 80$ collocation points have been used in the spanwise direction. Note that with this highest discretization used, the operator $\boldsymbol{A}$ in (4.9) is a $93\,132 \times 93\,132$ matrix and it would be impossible to apply a direct matrix-eigenvalue solver to the system. It has become customary to solve such large eigenvalue problems using Krylov subspace projection method together with a shift-and-invert strategy, known as the Arnoldi algorithm (see Nayar & Ortega 1993). Here, this approach is applied, similar to the global mode analysis in detached boundary layers performed in Gallaire, Marquillie & Ehrenstein (2007). Given the computer memory requirements (up to 140 Gbytes), most of the computations have been performed on the parallel shared memory IBM Power 6 cluster of IDRIS.

For validation, the results reported in Kawahara *et al.* (1998) for a modelled mean velocity and streak structure reminiscent of a low-Reynolds-number turbulent channel at $Re_\tau = 180$ have been considered. In this work, eigenmodes, referred to as modes I, II and III, are discussed in detail. For instance, the growth rate associated with the (sinuous) mode II, for a spanwise width 0.58 and dimensionless channel-height 2, reported in Kawahara *et al.* (1998) and converged within 4 % is $\omega_i = 0.6$, the real phase velocity being $c_r = \omega_r/\alpha = 13.6$. This result is retrieved in our computation (within the convergence error) for $N_y = 150$, $N_z = 20$, the computed value being $\omega_i = 0.63$ and $c_r = 13.4$.

4.4. *Stability results*

The streaks obtained using our detection procedure for the channel flow are shown in figure 11. Superimposing the averaged streak structure at $Re_\tau = 550$ (corresponding to $Re = 11\,180$ in the stability system (4.4)–(4.6)) to the mean velocity profile, the stability computations have been performed: no instability could be detected when considering the unconditionally averaged streaks. This is in agreement with previous investigations, which reported evidence of a streak-amplitude threshold for streak instability (see Elofsson *et al.* 1999; Schoppa & Hussain 2002) in near-wall turbulence. Critical amplitudes for instability of large-scale optimal streaks, solution of the Reynolds-averaged Navier–Stokes equation, have also been reported recently by Park, Hwang & Cossu (2011). The streak amplitude may however not be the only relevant parameter for streak breakdown and, for instance, secondary transient growth associated with optimal perturbations of streaks can be dominant (Schoppa & Hussain 2002; Hoepffner *et al.* 2005).

As discussed in § 4.2, there is some arbitrariness when defining the streaks intensity. When considering only the 10% strongest streaks according to both the A and θ criteria, no instability is found for the present turbulent channel flow, whereas for the I_s-criterion an instability threshold could be detected. The corresponding results are shown in figure 12, the + and × symbols being the amplification rates ω_i, as function of the perturbation wavelength λ^+, for the 20% and the 10% most intense streaks, respectively. As can be seen, the 20% most intense streaks are still stable, whereas the 10% strongest streaks have positive amplification rates for a range of wavelengths. The channel-half height being the reference length in the stability system (4.4)–(4.7), in wall-coordinates $\lambda^+ = 2\pi Re_\tau/\alpha$ with α being the streamwise wavenumber in (4.3).

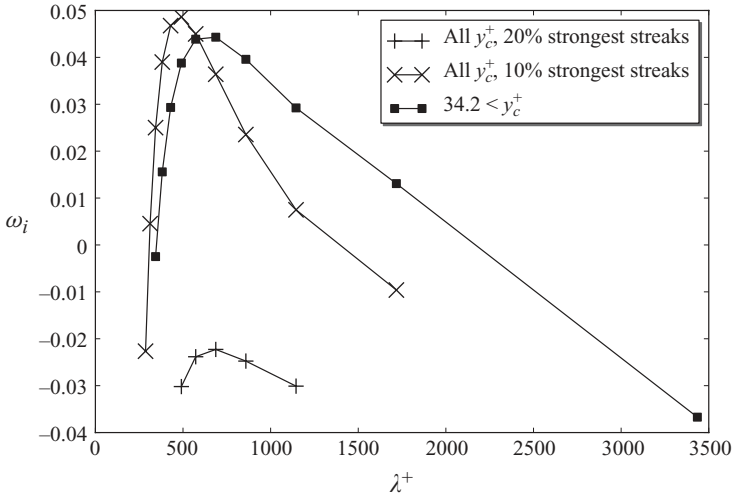

FIGURE 12. Channel streak instability growth rate ω_i as a function of the wavenumber λ^+ in wall units for the 20% strongest streaks (+), the 10% strongest streaks (×) (I_s-criterion, (4.2)) and the 20% highest streaks (■).

The computations have been performed for the highly resolved stability system with $N_y = 300$, $N_z = 80$, the spanwise width of the conditionally averaged streaks being $-0.307 \leqslant z \leqslant 0.307$ (or, equivalently, in wall coordinates $-169 \leqslant z^+ \leqslant 169$).

As already mentioned in § 4.2, an alternative criterion is to consider the distance of the streak's centre from the wall, the average of the 20% highest streaks being shown in figure 11. Using this conditionally averaged streak for the streak base flow, the stability characteristics have been computed as well and the results are shown in figure 12 (squares). The amplification rates are seen to be of the same order of magnitude, with again a maximum at $\lambda^+ \approx 500$, as those for the 10% most intense streaks. However, as can be inferred from figure 11, the average of the 20% highest streaks is less intense than the average of the 10% strongest streaks with respect to the I_s-criterion. Sets of streaks with centres closer to the wall have been considered as well, but the resulting streak base flows proved to be stable. It may therefore be hypothesized that the distance of the streaks from the wall may indeed be an alternative criterion when addressing the question of streak instability. The instability found for the most intense and the highest streaks is of sinuous type. The real part of the streamwise vorticity mode $\hat{\omega}_x = \partial\hat{w}/\partial y - \partial\hat{v}/\partial z$ (at the most unstable wavelength $\lambda^+ \approx 500$ for the 10% strongest streaks) is shown in figure 14. Note that for a sinuous perturbation, $\hat{\omega}_x$ is symmetric with respect to $z = 0$. In Schoppa & Hussain (2002), it has already been shown that sufficiently intense low-speed streaks in zero-pressure-gradient wall-turbulence become unstable to sinuous normal modes. The general sinuous scenario has also been addressed in the context of bypass transition for zero-pressure-gradient boundary-layer flows (see Schlatter *et al.* 2008). The symmetry properties of the streak instability mode are expected to be related to the inflection points of the base flow. It has, for instance, been shown (see Asai *et al.* 2002) that spanwise inflection points promote spanwise oscillations of the streaks, associated with the sinuous mode. The streak superimposed to the mean velocity profile, i.e. the streak base flow, is shown in figure 13 for the averaged streak as well as for the 10% strongest and the 20% highest streaks (the latter two base flows being unstable

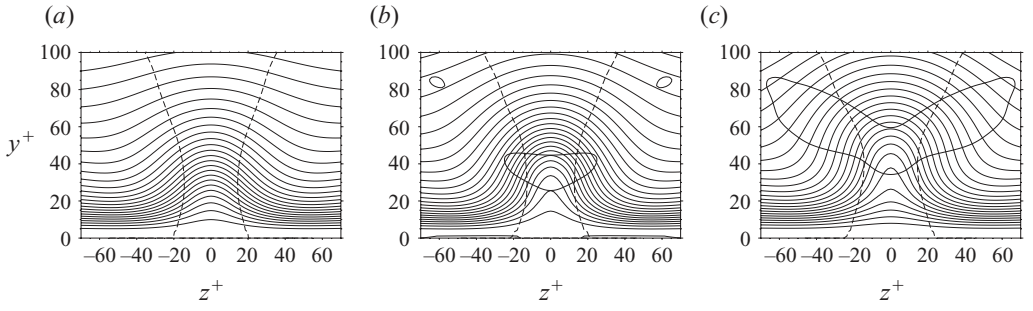

FIGURE 13. Contour plot of streak base flows for the flat channel at $Re_\tau = 550$: unconditionally averaged streaks (a), the average of the 10% strongest streaks (b) (I_s-criterion, (4.2)), the average of the 20% highest streaks (c). The thick continuous line and thick dashed lines indicate the location of $\partial^2\bar{U}/\partial^2 y = 0$ and $\partial^2\bar{U}/\partial^2 z = 0$, respectively.

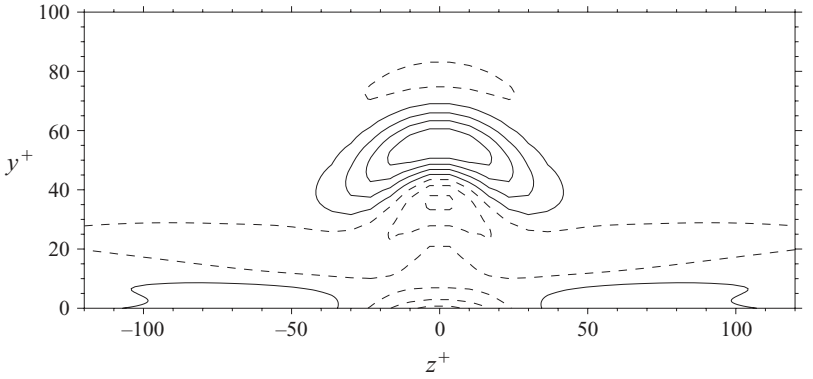

FIGURE 14. Real part of the most unstable perturbation streamwise vorticity mode $\hat{\omega}_x$, with $\lambda^+ \approx 500$, for the 10% strongest streaks of the flat channel at $Re_\tau = 550$ (see figure 12).

according to the results in figure 12). For the three cases, the location of the inflection points with respect to the spanwise coordinate (shown as the dashed lines) is very similar. For the strongest and highest streaks however, there is a closed contour of inflection points (shown as the thick continuous line) with respect to the wall-normal coordinate. This contour is centred at $y^+ \approx 40$ for the 10% most intense streaks. Interestingly, the iso-contours of the streamwise vorticity are precisely localized above and below $y^+ \approx 40$ as shown in figure 14.

5. Adverse-pressure-gradient turbulent flow

Owing to the non-parallel converging–diverging channel and the resulting pressure gradients, the averaged flow quantities, and, in particular, the streak base flow $\bar{U}$ in the stability system (4.4)–(4.6), depend on the streamwise coordinate x. Consequently, a normal-mode analysis assuming homogeneity of the disturbance in the streamwise direction is strictly speaking not valid anymore. When using the matrix-eigenvalue stability approach, it would however be hardly feasible to consider a full stability analysis for a base flow depending on the three space coordinates, given the computer memory requirements. Indeed, already for the parallel flow assumption, the stability operator is of very large size, the sharp gradients of the base flow near the wall necessitating a high resolution in (y, z) (which at each x location is the

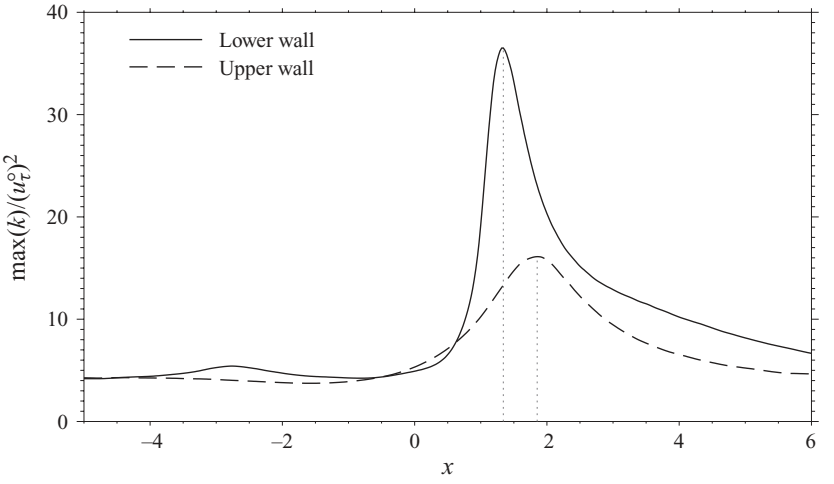

FIGURE 15. Streamwise evolution of the maximum turbulent kinetic energy peak at the two walls of the converging–diverging channel flow.

coordinate system normal to the wall which is considered). It is only *a posteriori*, by assessing the instability findings in relation to the flow simulation results, that the locally parallel base flow assumption will find some justification. The appropriate locations for significant local streak instability analyses have to be inferred from some characteristics of the turbulent flow field, assuming that indeed streak instability is associated with the generation of near-wall streamwise vortices.

5.1. *Vortices and turbulent kinetic energy*

The Q-criterion depicted in figure 6 indicates a sudden increase of turbulence at some location slightly downstream the bump, which is confirmed by the increase of turbulent kinetic energy shown in figure 15. Indeed, a rather sharp dominant peak is visible at the lower wall starting at a small distance from $x = 0$ (the bump summit), while slightly more downstream a smoother peak can be seen for the upper wall.

The dominant role of the streak near the upper wall is retrieved in the Q-criterion for the direct numerical simulation results, shown in figure 16. The intense vortices are seen to precisely emerge from the streak skeletons upstream and the structures are irregularly distributed in the spanwise direction. The definite breakdown of streaks at the upper wall takes place within a certain range in the streamwise coordinate, rather than at a precise x-value and the emerging structures, which are confined in a limited bandwidth, travel some distance downstream.

Owing to the non-homogeneity in the streamwise x-direction, in the following two sets of wall units are considered. Local wall units are denoted conventionally with the superscript $+$ and reference wall units based on u_τ° at the inlet have the superscript $\star$. In order to quantify the correlation between the low-speed streaks and the vortices visualized in figure 16, the conditional probability, with respect to the streaks spanwise location, for the presence of intense vortices at a given position in the (y, z) plane is considered. For the correlation analysis, the intense vortices have been defined as the region in space where the Q-criterion is larger then a constant value ($Q > 200$) and the statistics are computed for all low-speed streak centres at a fixed streamwise location. This correlation statistics is shown in figure 17 for the upper wall at $x = 2.01$ in the region corresponding to the peak of turbulent kinetic energy. The correlation between

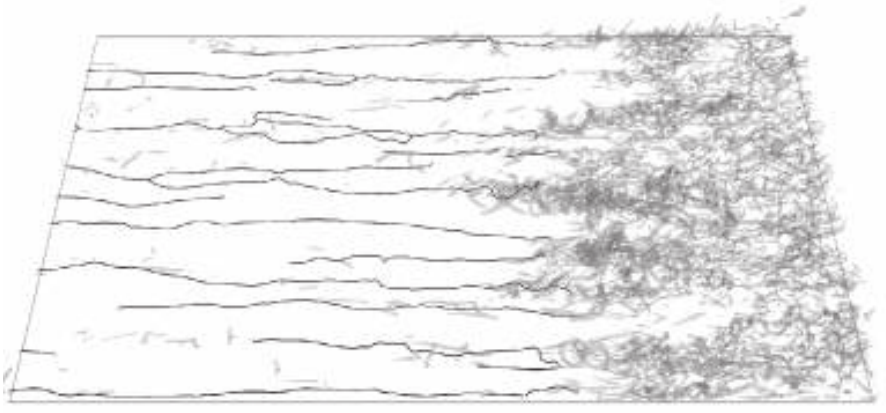

FIGURE 16. Iso value of the Q-criterion and skeleton of the low-speed streaks at the upper wall in the region of instability ($1.7 < x < 4.2$)

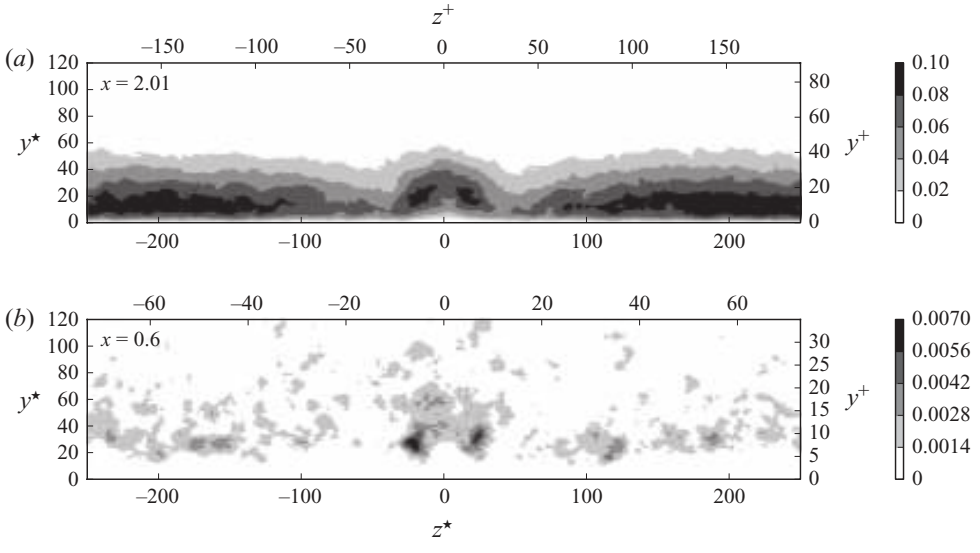

FIGURE 17. Probability density function of vortices (defined as region of space where $Q > 200$) conditioned by the presence of a low-speed streak at $z^\star = 0$. Upper wall statistics at $x = 2.01$ (a) and lower wall statistics at $x = 0.6$ (b).

the streaks and intense vortices is larger around the streak centres. Its value exhibits a maximum at the two sides of the streaks which may be the mark of counter-rotating vortices associated with varicose mode instability. A strong correlation also appears away from the streak centres which is due to the quasi-periodicity of streaks in the spanwise direction. The same statistics were conducted at the lower wall at $x = 0.6$, the production of intense vortices being much more localized in the streamwise direction than for the upper wall. This indicates that if the vortices emerge through streaks breakdown, they rapidly spread homogeneously in the spanwise direction as can be seen in figure 6. However, upstream this position, the correlation between streaks and vortices exhibits two peaks at each side of the streaks, as seen in figure 17. The correlation is much weaker than for the upper wall as the statistics are conducted

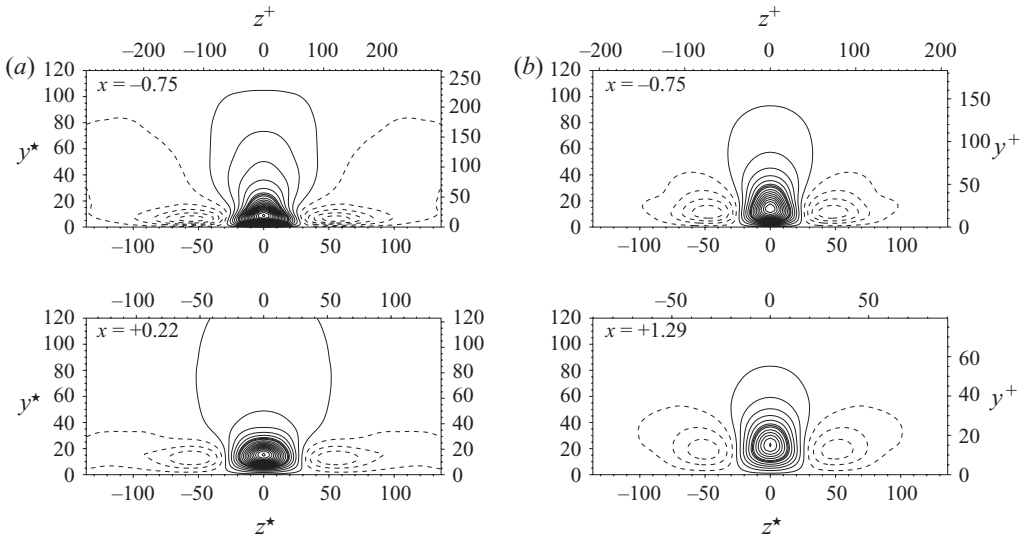

FIGURE 18. Averaged streaks $\langle u' \rangle_x$ at two streamwise locations x at the bottom wall (a) and upper wall (b) of the converging–diverging channel. The streaks are visualized with negative (continuous lines) and positive (dashed lines) iso-contours (increment 0.15 u_m^{rms}) of conditional average of the fluctuating streamwise velocity in the vicinity of low-speed streaks detected using the procedure described in § 3. The iso-contour corresponding to the detection threshold ($u' = -0.9\ u_m^{rms}$) is plotted with a continuous thick line.

at a streamwise position which is located at the beginning of the peak of kinetic energy, indicating that only a small fraction of vortices are generated. The maximum correlation increases further downstream (not shown here) but it becomes nearly homogeneous in the spanwise direction.

5.2. *Characterization of low-speed streaks*

The same detection procedure is used to compute the average statistics at each streamwise location of the two walls of the APG channel flow DNS. The shape of the averaged streaks is compared at two locations for each wall (see figure 18). The first position ($x = -0.75$) is located in the converging part of the flow near the maximum peak of C_f. The second positions are located near the minimum of C_f at each wall. The shapes in the converging part ($x = -0.75$) are rather different at the two walls. At the lower wall, the streak is distorted by the effect of the strong favourable pressure gradient to reach a triangular-like shape with a large lower basis. With a lower favourable pressure gradient, the structure is much less distorted at the upper flat wall but is slightly reshaped as compared to the average streak in the flat-channel flow.

The size and position of the average streaks for the two walls are shown in figures 19 and 20. The statistics are indicated both in reference wall units and in local wall units in order to be able to compare the streamwise physical modifications at different streamwise locations. At the lower wall, the average width is nearly constant in reference wall units ($l_z^\star \simeq 27$) up to $x = 0.4$. The growth of $l_z^\star$ further downstream is probably not significant as it is located downstream the separation point where most of streaks are destroyed (see figure 8). The average height $l_y^\star$ presents a minimum near $x = -0.4$ which corresponds roughly to the beginning of the adverse-pressure-gradient

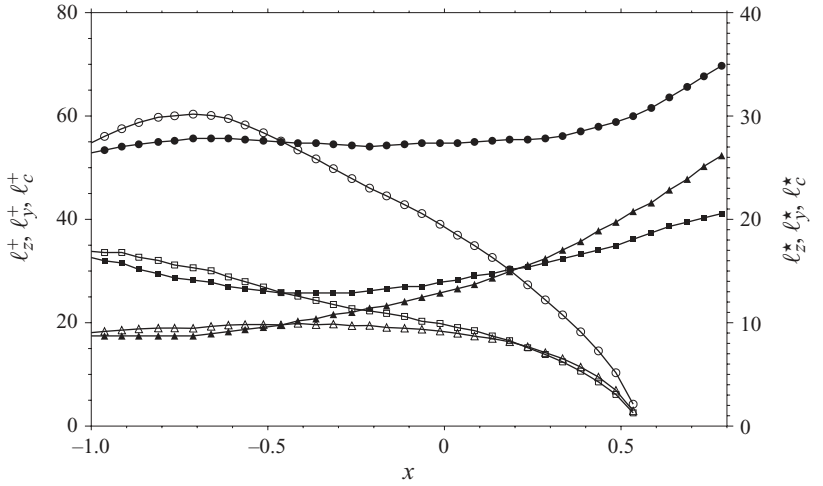

FIGURE 19. Streamwise evolution of the statistics of averaged streaks $\langle u' \rangle_x$ at the lower wall of the converging–diverging channel. The width l_z (circles), height l_y (squares) and distance of the centre l_c from the wall (triangles) are plotted in local wall units (open symbols, left scale) and in inlet reference wall units (filled symbols, right scale).

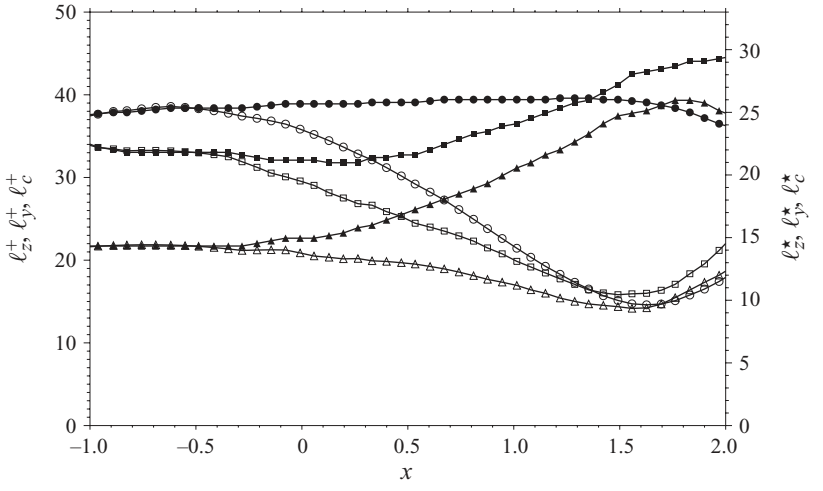

FIGURE 20. Streamwise evolution of the statistics of averaged streaks $\langle u' \rangle_x$ at the upper wall of the converging–diverging channel. The width l_z (circles), height l_y (squares) and distance of the centre l_c from the wall (triangles) are plotted in local wall units (open symbols, left scale) and in inlet reference wall units (filled symbols, right scale).

regime. The centre of streaks starts to move away from the wall further upstream in reference wall units ($l_c^\star$) but stays almost constant in local wall units ($l_c^+ \simeq 20$) down to the summit of the bump. The statistics of the average streak behave similarly at the upper wall but the curves are shifted downstream following the shift of the pressure gradient curve (see figure 3). For instance, the minimum of the streak height $l_y^\star$ is located near $x = 0.2$ which also corresponds to the beginning of the adverse pressure gradient at the upper wall.

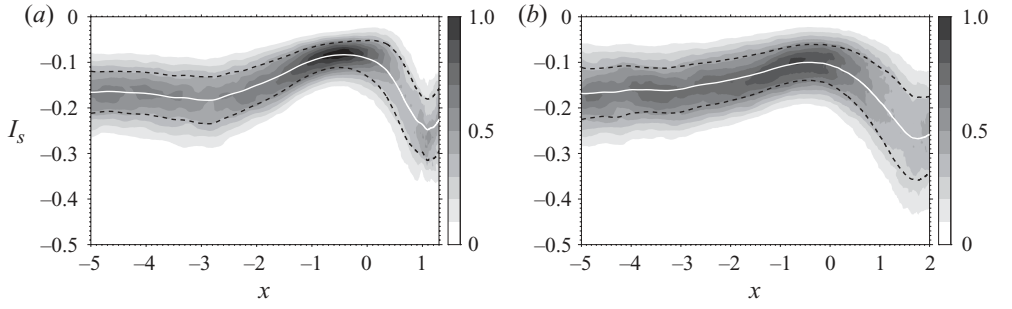

FIGURE 21. Streamwise evolution of the probability density function of the low-speed streaks intensity at the lower wall (*a*) and the upper wall (*b*) evaluated with the I_s-criterion. The results are normalized by the maximum value of the probability along x. The average intensity is indicated with a solid white line and the two black dash lines correspond to $\pm$ 1 standard deviation.

Similar to the channel flow case, the probability of the low-speed streaks intensity has been investigated using the I_s criterion. The streamwise evolution of the probability density function is shown for each wall in figure 21. The statistics exhibit similar behaviour at the two walls. The streaks intensity increases smoothly in the region of favourable pressure gradient and decreases rapidly under adverse pressure gradients. The weakening of streaks intensity coincides approximately with the lift up of their centre as noticed in figures 19 and 20. This seems to confirm that the intensity and the wall distance of the streaks are rather correlated.

5.3. *Pressure-gradient streak instability*

Superimposing the respective mean flow profiles to the streak averages, the stability computations have been performed for the resulting streak base flow $\bar{U}(y, z)$ nearby the region of the turbulent kinetic energy peaks, i.e. around $x = 0.22$ for the lower streaks and in the vicinity of $x = 1.29$ for the upper streak. The domain $-0.218 \leqslant z \leqslant 0.218, 0 \leqslant y \leqslant 1$ used for the stability computations (or, equivalently, in reference wall units $-134.5 \leqslant z^\star \leqslant 134.5$, $0 \leqslant y^\star \leqslant 617$) corresponds to the spanwise-box for the detected streaks shown in figure 18. It has been checked that using $N_y = 300$ and $N_z = 50$ collocation points in y and z, respectively, yields converged stability results to three digits in the amplification rate ω_i. The Reynolds number used in the stability system is according to the turbulent flow simulations $Re = 12\,600$.

5.3.1. *Upper wall streaks instability*

As discussed in the case of the turbulent channel flow, the different criteria based on the intensity of the low-speed streaks are somewhat arbitrary. In particular, no clear connection between the intensity and a possible instability of streaks could be assessed. The results seem however to indicate that the distance of the streak centre from the wall may be an alternative criterion. By assuming that the regions of the turbulent kinetic energy peaks in figure 15 are also those where the streak base flow may be unstable, the streak base flows have been computed at $x = 1.29$. Figure 22 shows the base flows corresponding to the average of sets of streaks formed according to their distances from the wall. Five distinct sets have been considered, labelled S_1–S_5, each one containing 20% of the streaks ranged according to increasing distance from the wall (with S_1 the 20% closest, S_2 the 20–40% closest, etc. and S_5 the 20% highest streaks). The lines of inflection points are drawn as well and for all five sets of streaks considered the spatial distribution of the inflection points with respect to z is similar.

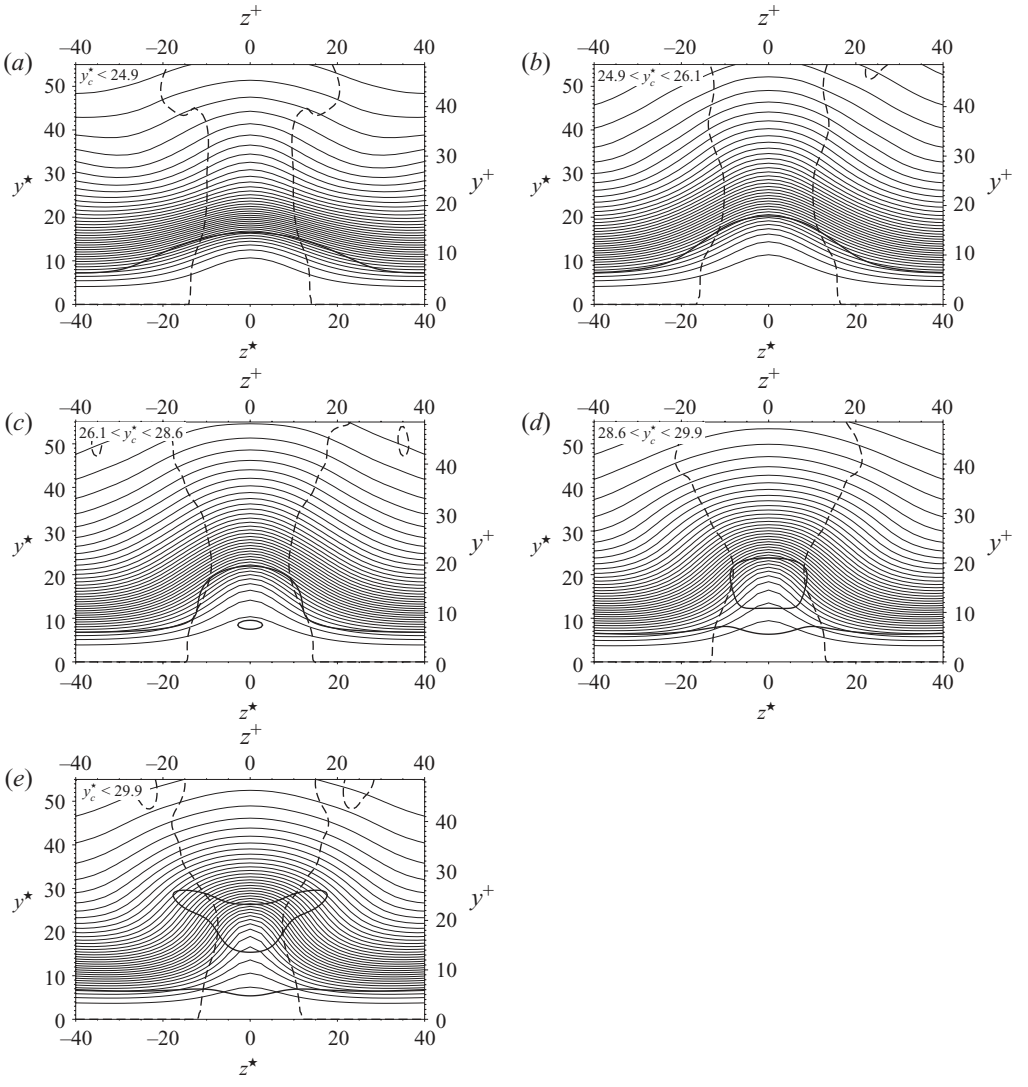

FIGURE 22. Contour plot of upper streak base flow at $x = 1.29$, for the conditional average using the distance of the streak's centre $y_c^\star$ from the wall. Five distinct sets have been considered, labelled S_1–S_5, each one containing 20% of the streaks ranged according to increasing distance from the wall, S_1 being the 20% closest, S_2 the 20–40% closest, etc. and S_5 the 20% highest streaks. S_1 (*a*), S_2 (*b*), S_3 (*c*), S_4 (*d*), S_5 (*e*). The thick continuous line and thick dash lines indicate the location of $\partial^2\bar{U}/\partial^2 y = 0$ and $\partial^2\bar{U}/\partial^2 z = 0$, respectively.

However, differences occur for the inflection points with respect to the wall-normal coordinate. While for the sets with streaks closest to the wall there is only one more or less distorted line of inflectional points with respect to y close to the wall, for higher streaks a second closed contour appears.

Figure 23 depicts the corresponding stability results and it can be seen that the different streak base flows are indeed unstable. The most unstable streaks are those closest to the wall and interestingly there is an unstable varicose as well as an unstable sinuous mode. However, the maximum of the amplification rate of the varicose

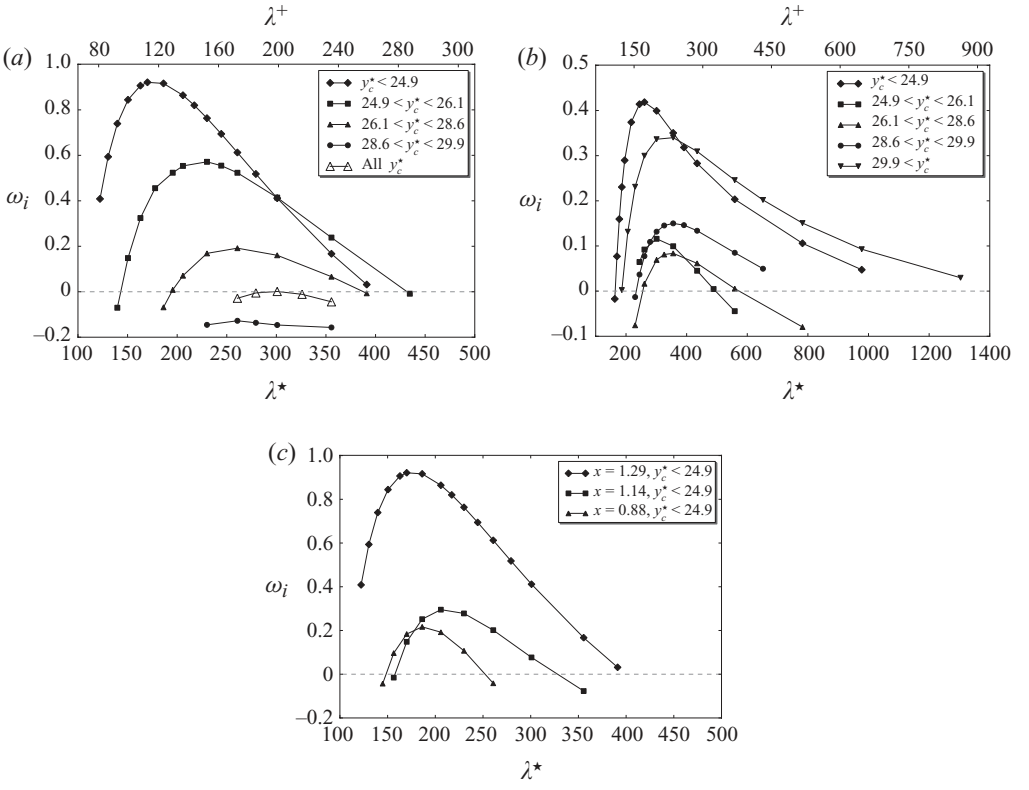

FIGURE 23. Streak instability growth rate ω_i at the upper wall, for conditionally averaged streak base flows, with respect to the streak's distance from the wall, as function of the wavelength in reference wall units ($\lambda^\star$) and (λ^+). Streak base flow at $x = 1.29$; varicose instability (a), sinuous instability (b), for set S_1 (20% closest streaks ◆), set S_2 (20–40% closest streaks ■), set S_3 (▲), set S_4 (●), set S_5 (20% highest streaks ▼). Varicose instability for total average of streaks (△). (c): varicose instability for the average of the 20% lowest streaks at $x = 0.88$ (▲), $x = 1.14$ (■) and $x = 1.29$ (◆).

mode is about twice as high as its sinuous counterpart. When increasing the distance from the wall, the amplification rates of the varicose mode decrease and the streaks corresponding to set S_4 are stable to varicose instability. The behaviour is different for the instability of sinuous type. All five different streak base states are unstable, the 20% closest streaks and the 20% highest streaks being unstable with comparable amplification rates, as can be seen in figure 23. The total average of all the streaks has been considered as well: in that case, only (an almost neutral) instability of varicose type could be found (see △ in figure 23a).

Focusing on the most unstable streak base flow formed with the average of the 20% streaks closest to the wall, the varicose instability, which is the dominant one, has been computed for base flows upstream. As shown in figure 23, the instability weakens upstream but is still present at $x = 0.88$ with however low amplification rates. It is interesting to note that this location is close to the increase of the turbulent kinetic energy at the upper wall (see figure 15).

These results clearly demonstrate that the streak's distance from the wall is a particularly sensitive parameter in connection with streak instability. Note that for the present adverse-pressure-gradient wall turbulence, the base flow with the average

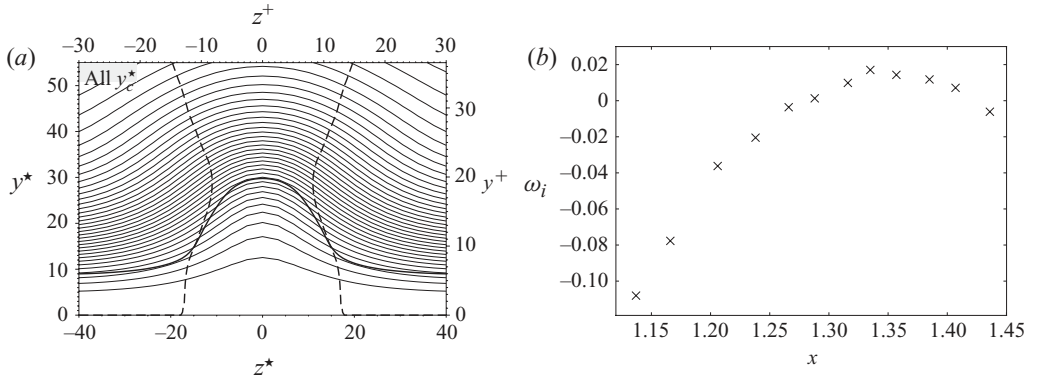

FIGURE 24. Unconditionally averaged streak base flow at $x = 1.29$ (a). Growth rate ω_i of the varicose mode at fixed wavelength $\lambda^\star \approx 300$ at different x-locations for the unconditionally averaged streak base flow (b).

of all the streaks is itself unstable, with respect to the varicose mode. This base flow is shown in figure 24 (a) for $x = 1.29$ and the amplification rates are shown as well, for this unconditionally averaged streak base flow at different x locations for a fixed perturbation wavelength $\lambda^\star \approx 300$ (which corresponds to the neutral instability result at $x \approx 1.29$, see figure 23). The total average base flow is seen to become stable slightly upstream at $x = 1.29$.

Isolines of the unstable mode structure are shown in figure 25, the real part of the streamwise velocity component $\hat{u}$ being depicted for both the varicose as well as sinuous mode, for the base flow with the 20% lowest streaks at $x = 1.29$. The wavenumber is $\lambda^\star = 185$, the corresponding amplification rates being $\omega_i = 0.92$ and $\omega_i = 0.23$ (see figure 23). Figure 26 exhibits the corresponding three-dimensional perturbation structures over one streamwise wavelength, the streamwise component of the vorticity and the Q-criterion isosurface being shown. The vortex structure of the varicose perturbation is counter-rotating and the Q-criterion isosurface is seen to have a nice horseshoe-type structure.

5.3.2. *Lower wall streak instability*

The turbulent kinetic energy evolution along the lower wall with the bump exhibits a peak only slightly downstream the bump summit (see figure 15) and this region is explored addressing again the possibility of streak instability. Streak base flows at $x = 0.22$ are depicted in figure 27 with the average of the 20% lowest streaks as well as the 20% highest streaks. In contrast with the results at the upper wall, the inflection points with respect to the wall-normal coordinate are almost homogeneously distributed along the spanwise coordinate. The streak base flows using the other sets of conditionally averaged streaks, using the distance criterion, as well as the total average of the streaks look very similar and are not depicted here. This indicates that at the lower wall, the inflectional mean velocity profile is the dominant part in the streak base flow. The stability analysis (using again $N_y = 300$ and $N_z = 50$ collocation points) has been performed and the results are depicted in figure 28. Only varicose modes become unstable and the highest amplification rates ω_i are reached for the average with the streaks closest to the wall. Considering the 20–40% lowest streaks, the corresponding base flow is seen to be almost marginally stable and for averages with higher streaks the amplification rates again slightly increase at somewhat lower

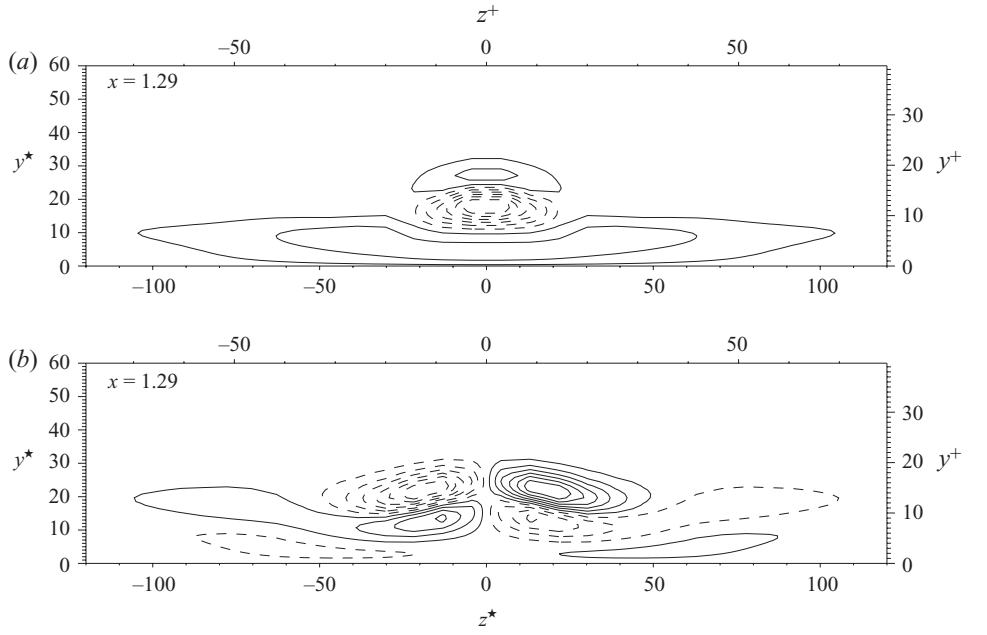

FIGURE 25. Real part of the streamwise perturbation velocity mode $\hat{u}$ at $\lambda^\star = 185$ for the conditionally averaged streak base flow with the 20% streaks closest to the wall at $x = 1.29$ at the upper wall (see figure 23). Varicose mode (a) and sinuous mode (b).

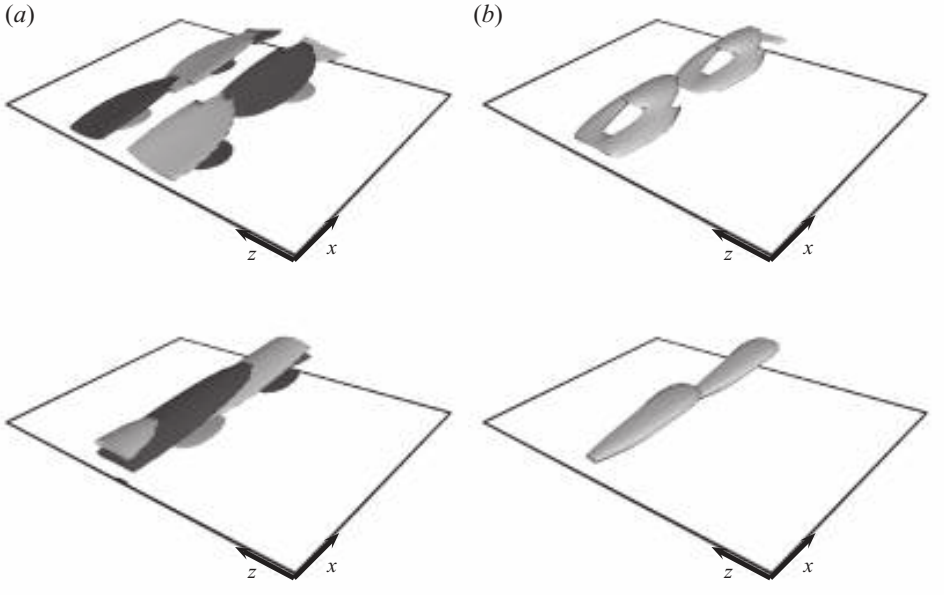

FIGURE 26. Three-dimensional structure of the streak perturbation at $x = 1.29$ upper wall and $\lambda^\star \approx 185$ (see figure 23). Isosurface ($\pm 6.8\ \omega_x^{rms}$) of the perturbation streamwise vorticity (a) and Q-criterion isosurface (b) for the varicose instability (top) and sinuous instability (bottom).

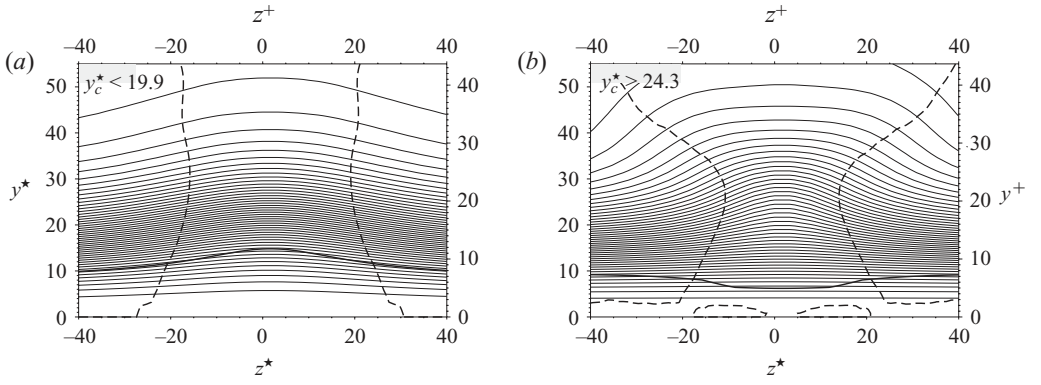

FIGURE 27. Contour plot of streak base flow near the lower wall at $x = 0.22$ for conditionally averaged streak base flow with the 20% lowest streaks (a) and 20% highest streaks (b). The thick continuous line and thick dash lines indicate the location of $\partial^2\bar{U}/\partial^2 y = 0$ and $\partial^2\bar{U}/\partial^2 z = 0$, respectively.

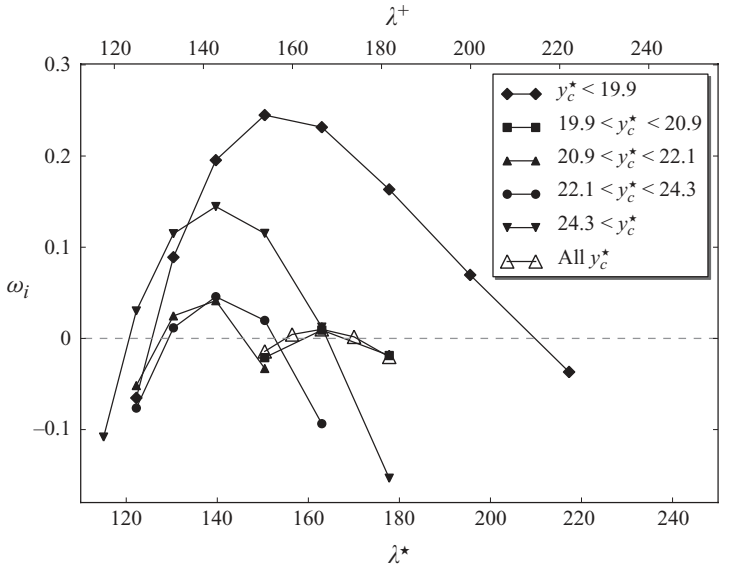

FIGURE 28. Streak instability growth rate ω_i at the lower wall at $x = 0.22$ for conditionally averaged streak base flows, with respect to the streak's distance $y_c^\star$ from the wall, as function of the wavelength in wall units ($\lambda^\star$) and (λ^+). Set S_1 (20% closest ◆), set S_2 (20–40% closest ■), set S_3 (▲), set S_4 (●) and set S_5 (20% highest ▼). Total average (△).

wavelengths. The result for the average with the total set of streaks is also depicted (△ in figure 28) and is seen to be marginally stable. The perturbation streamwise velocity mode for the streak base flow with the total average is depicted in figure 29, for the most unstableperturbation wavelength $\lambda^\star \approx 161$ (or, equivalently, $\alpha = 24$). The almost homogeneous structure in z, besides the region near the centre, again represents the footprint of the dominant mean velocity profile. The perturbation streamwise vorticity mode is depicted as well. This mode structure is located very close to the wall and has a finite width in the spanwise box, the structure being governed by the streak component in the base flow which gives rise to a three-dimensional perturbation structure. The

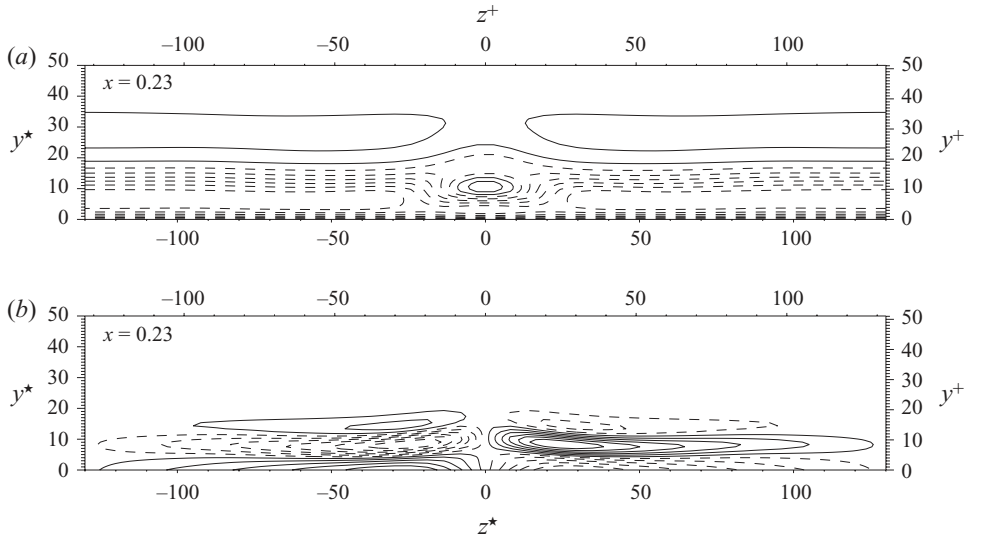

FIGURE 29. Most unstable perturbation for the total averaged streak base flow at the lower wall at $x = 0.22$ for the perturbation wavelength $\lambda^\star \approx 161$ (see figure 28). Perturbation streamwise velocity mode $\hat{u}$ (a), perturbation streamwise vorticity mode $\hat{\omega}_x$ (b).

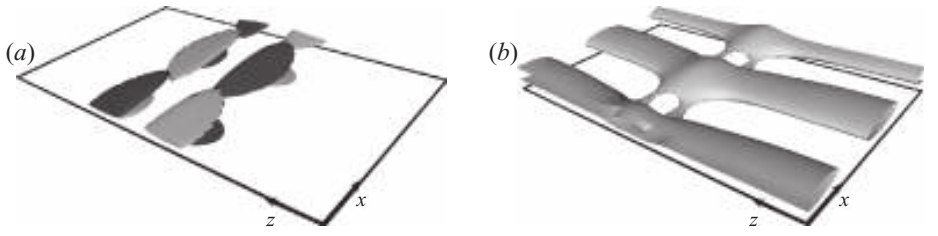

FIGURE 30. Three-dimensional structure of the almost-neutral lower streak perturbation at $x = 0.22$ and $\lambda^\star \approx 161$ (see figure 28). Isosurface ($\pm 8.5\ \omega_x^{rms}$) of the perturbation streamwise vorticity (a) and Q-criterion isosurface (b).

instability being varicose, the streamwise vorticity is anti-symmetric with respect to $z = 0$, whereas the streamwise velocity component is symmetric. The corresponding three-dimensional perturbation structure over one streamwise wavelength is shown in figure 30. In contrast with the varicose perturbation at the upper wall (see figure 26), the Q-isosurface is homogeneously distributed in the spanwise direction, again as the consequence of the dominant mean velocity profile which generates homogeneous (in z) spanwise vorticity.

To precisely assess the unstable character of the mean velocity profile component $U(y)$ in the streak base flow, a one-dimensional stability computation has been performed, using $U(y)$ as base flow (i.e. for the stability system of Orr–Sommerfeld type, computing the modes depending only on y). The results at different x locations are depicted in figure 31 (+) and the mean velocity profile is indeed unstable. The amplification rates are compared with the streak base flow computations (×), using the total average of the streaks at the different x-locations at the lower wall. The wavelength has been fixed at $\lambda^\star \approx 160$ which is close to the most unstable wavenumber

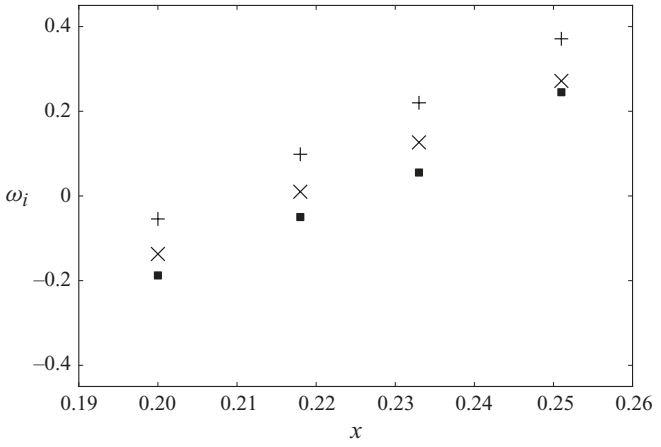

FIGURE 31. Instability growth rate ω_i at the most unstable wavelength $\lambda^\star \approx 160$ at different x-locations for the lower streak base flow ($\times$). $+$: growth rates for the one-dimensional mean velocity profiles. ■: growth rates for the one-dimensional mean velocity profiles with $\nu_T(y)$.

for the total average streak. The growth rates are seen to increase almost linearly with x, the mean base flow being slightly more unstable than the streak base flow.

It has to be emphasized that, contrary to the lower wall result, the mean velocity profiles at the upper wall proved to be stable. This may be attributed to the weaker adverse pressure gradient at the upper wall. The slope of the wall-normal derivative of the mean streamwise velocity at different x locations at the lower wall is depicted in figure 32, showing that a pronounced local maximum (the inflection point) enters the flow domain downstream the bump summit $x = 0$. At the upper wall however, the profile-slope maximum (not depicted) is less pronounced and remains much more in the vicinity of the wall.

Recently, mean flow stability computations have been performed in turbulent boundary layers by Cossu, Pujals & Depardon (2009) or in the turbulent channel flow by del Álamo & Jiménez (2006), adding an eddy-viscosity in the stability equations for the turbulent mean velocity profile. Such models have been analysed in the past for instance by Reynolds & Hussain (1972). The eddy-viscosity $\nu_T(y)$ is used instead of the Reynolds stress in this model and it is the solution of (by considering the averaged streamwise momentum equation)

$$\left(\frac{1}{Re} + \nu_T(y)\right)\frac{\partial U}{\partial y} = u_\tau^2 + \int_0^y \left(U\frac{\partial U}{\partial x} + V\frac{\partial U}{\partial y} + \frac{\partial P}{\partial x}\right). \tag{5.1}$$

In the present investigation, all mean quantities are available and the $\nu_T(y)$ profile can be computed. A similar approach to compute $\nu_T(y)$ for a modelled turbulent boundary layer (without pressure gradient) is used in Cossu *et al.* (2009).

For the data in the vicinity of $x = 0.22$, the $\nu_T(y)$ increases up to $y^\star \approx 80$ in reference wall units and has been kept constant outside this inner region. The results of the stability computations adding $\nu_T(y)$ are shown in figure 31 (filled square). The eddy-viscosity is seen to slightly damp the perturbation, the results being however similar to those considering only the molecular viscosity in the stability equations. It is however doubtful that there is a rational grounding to use $\nu_T(y)$ when considering a streak base flow depending on y and z. Therefore, in the present investigation, only the molecular viscosity associated with the Reynolds number, used in the direct

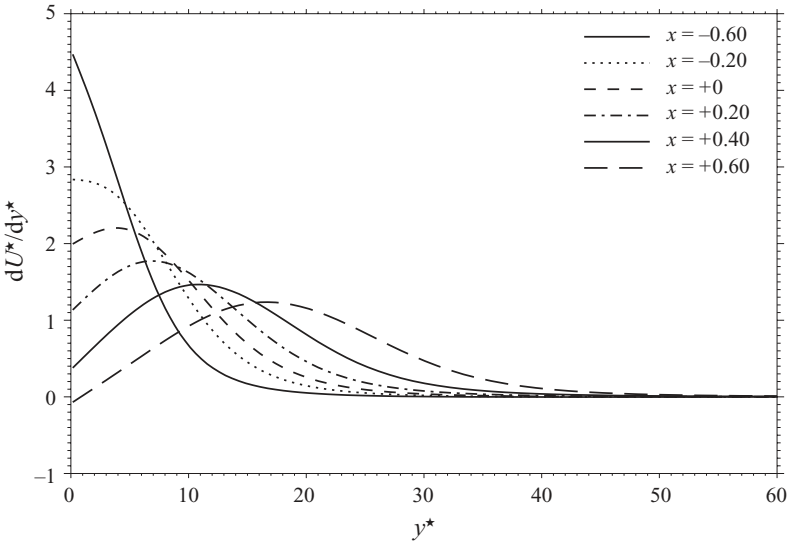

FIGURE 32. Profiles of the wall-normal derivative of the mean streamwise velocity at several streamwise positions at the lower wall.

numerical simulation, has been used for the streak base flow stability problem (as, for instance, in Schoppa & Hussain 2002).

6. Discussion and conclusions

For zero-gradient-pressure boundary layers, the structures resulting from streak instabilities have been addressed experimentally, among others, by Asai *et al.* (2002). There is evidence that symmetric (varicose) streak instability modes lead to the formation of hairpin vortices, whereas sinuous mode instabilities give rise to quasi-streamwise vortices with vorticity of alternate sign. More recently, Brandt & de Lange (2008) provided evidence for symmetric and antisymmetric breakdown due to streak interaction. In our curved channel flow, wall turbulence direct numerical simulation data are available for stronger, at the lower wall, and weaker adverse pressure gradients. Addressing streak instability and considering the total average of the streaks which have been detected, the streak base flows proved to become unstable at some streamwise location with respect to varicose modes. Considering however conditional averages for the streak base flow, using as a criterion the distance of the streak's centre from the wall, at the upper wall sinuous modes proved to become unstable too. At both walls, the averages of streaks the closest to the wall (the 20% closest) exhibit the highest amplification rates for varicose modes and there is evidence of a relation between the increase of the amplification rates when progressing along the wall and turbulent kinetic energy peaks observed in the direct numerical simulation results. At the upper wall, with the weaker adverse pressure gradient, the streak base flow with the average of the highest streaks exhibits wall-normal inflection point located on a closed contour in the (y, z) plane. In this respect, the base flow characteristics (see figure 22*d* and *e*) are reminiscent of the streak averages considering the most intense or the highest streaks in the turbulent zero-pressure-gradient channel flow (see figure 13) and only the sinuous mode prevails for these base flows. At the lower wall with the stronger adverse pressure gradient, only

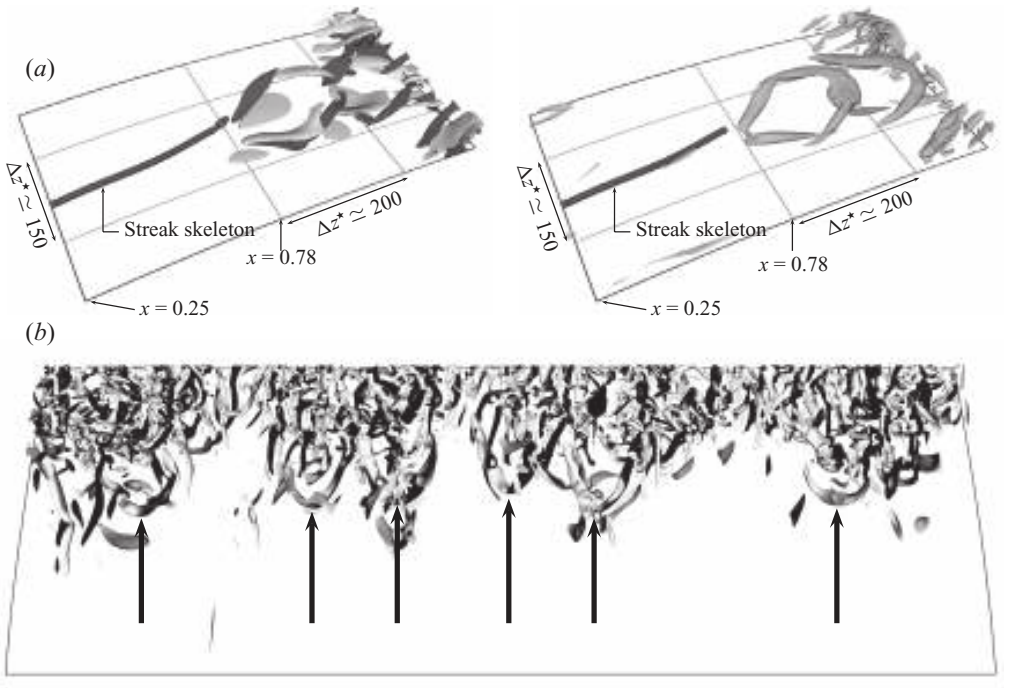

FIGURE 33. Visualization of a well-defined coherent structure at the lower wall in the region of instability. (*a*) streamwise vorticity with light grey colour for negative and dark grey colour for positive values (left); iso-value of the Q-criterion (right). A streak is present in front of the structures, a portion of which is being visualized with its skeleton. (*b*) coherent structure events along the spanwise direction for $0.4 \leqslant x \leqslant 1.41$ (the arrows point at Q-isosurfaces, coloured with the streamwise vorticity).

unstable varicose modes are found, no matter what average for the streak base flow is considered. Also, in that case, the instability increases precisely and quite abruptly at the x-location immediately prior to the dominant kinetic energy peak shown in figure 15. Three-dimensional structures have been extracted from the direct numerical simulation database and the result is shown in figure 33. An individual streak skeleton is depicted (figure 33*a*) near the lower wall and it appears to be the main coherent structure down to $x = 0.78$ where indeed a hairpin-type streamwise vortex emerges. The Q-isosurface is shown as well and there is hence evidence of symmetric (varicose) breakdown of the streak into a coherent structure of counter-rotating streamwise vortices. Very similar varicose structures have, for instance, been reported in Brandt, Schlatter & Henningson (2004) in a transitional boundary layer subject to free-stream turbulence. The sudden formation of hairpin-type vortices is a recurring event along the spanwise direction as seen in figure 33(*b*). Indeed, the arrows in the figure point at those structures, depicted as Q-isosurface coloured by the streamwise vorticity.

In our stability analysis, the streak instability starts at some distance upstream the location where the hairpin vortices emerge. Here, a temporal stability analysis has been performed using the locally parallel flow assumption. It is expected that the instability is of convective nature (see Brandt *et al.* 2003) and the temporal growth is hence in relation with a spatial growth. Consequently, the coherent structure has to grow to some amplitude downstream before it becomes visible in the simulation

results. The size of the hairpin vortex is approximately $\Delta x^\star \approx 200$, the spanwise width being $\Delta z^\star \approx 150$. Interestingly, this is the order of magnitude of both the spanwise size of the perturbation streamwise vorticity mode (depicted in figure 29) and the most unstable wavelength $\lambda^\star \approx 161$ (see figure 28).

The corresponding three-dimensional perturbation structure is shown in figure 30 and the streamwise vorticity distribution is seen to be reminiscent of the hairpin-type vortex structure detected in the simulation. The Q-criterion isosurface is depicted as well which however bears no resemblance to the turbulent quantity in the simulation (see figure 33). Indeed, as we have discussed previously, near the lower wall the mean velocity profile contributes to the instability which, in contrast to the real flow, artificially generates spanwise vorticity homogeneously distributed in the spanwise direction.

The attempt to clearly identify a precise location where coherent vortex structures, for instance, of hairpin-type, appear at the upper wall was less successful. At the upper wall, the instability is much more governed by the different possible averages considering specific sets of streaks. Furthermore, the stability analysis with the total streaks average predicts a less abrupt onset of instability at the upper wall, as seen in figure 24. An example of the three-dimensional perturbation structure is shown in figure 26, for a case where both a sinuous and a varicose mode is unstable. Both types of structures, the counter-rotating structure and the sinuous type with alternate vorticity, are likely to be tangled up in the direct numerical simulation data and can hardly be detected individually.

One may draw the general conclusion that in the APG flow considered, the turbulent kinetic energy exhibits characteristic peaks at both walls which clearly coincide with the production of intense coherent vortices. Indeed, the detection procedure shows that the turbulent flow field upstream the energy peak is marked by elongated low-speed streaks. Base flows formed with averages of the streaks superimposing the mean velocity profile become precisely unstable in the region of the energy peaks. However, there is no definite averaged streak base model, the type and strength of instability depending, in particular for the upper-wall weak pressure-gradient flow, on the specific set of streaks considered. In this respect, the streak's distance from the wall appears as an essential parameter. Of prime importance for the type of instability are the more or less homogeneously (with respect to the spanwise coordinate) distributed inflection points in the wall-normal coordinate for the streak base flow.

While at the upper wall (with a weaker pressure gradient), the stability results are dominated by the streak's contribution to the base flow, for the strong adverse pressure gradient near the lower curved wall the mean velocity component in the streak base flow also contributed to the sudden onset of the instability. These different stability results provide strong evidence that in the present APG wall turbulence, the averaged streak instability dynamics is related to the local onset of strong production of kinetic energy. This behaviour is different from what is observed for zero-pressure-gradient channel flow. In that case, modal instability is possible only for streaks extracted from the simulation data with some threshold amplitude, or for very specific set of streaks, and transient growth mechanisms possibly dominate (Schoppa & Hussain 2002; Asai *et al.* 2007).

One may conjecture whether the reported results are generic for adverse-pressure wall turbulence. Note that characteristic turbulent energy peaks seem to be a general feature in the presence of APG (see Shah *et al.* 2010). To connect this behaviour to streak breakdown will certainly have to be interpreted in the light of turbulence modelling. Indeed, the mean turbulent velocity gradients are at the heart of Reynolds-

averaged Navier–Stokes modelling, which is unlikely to be reliable in the presence of turbulence production peaks as a result of a streak instability mechanism.

This work was supported by WALLTURB (A European Synergy for the Assessment of Wall Turbulence) which is funded by the EC under the 6th framework program (CONTRACT: AST4-CT-2005-516008) and CISIT (International Campus on Safety and Intermodality in Transport). The DNS was performed through two successive DEISA Extreme Computing Initiatives (DEISA is a Distributed European Infrastructure for Supercomputing Applications). This work was granted access to the HPC resources of IDRIS under the allocation 2010-021741 made by GENCI (Grand Equipement National de Calcul Intensif). The authors are grateful for helpful discussions with Professor Michel Stanislas.

REFERENCES

Acarlar, M. S. & Smith, C. R. 1987 A study of hairpin vortices in a laminar boundary layer. Part 2. Hairpin vortices generated by fluid injection. *J. Fluid Mech.* **175**, 43–83.

del Álamo, J. C. & Jiménez, J. 2003 Spectra of the very large anisotropic scales in turbulent channels. *Phys. Fluids* **15** (6), L41–L44.

del Álamo, J. C. & Jiménez, J. 2006 Linear energy amplification in turbulent channels. *J. Fluid Mech.* **559**, 205–213.

del Álamo, J. C., Jiménez, J., Zandonade, P. & Moser, R. D. 2004 Scaling of the energy spectra of turbulent channels. *J. Fluid Mech.* **500**, 135–144.

Andersson, P., Brandt, L., Henningsson, D. S. & Bottaro, A. 2001 On the breakdown of boundary layer streaks. *J. Fluid Mech.* **428**, 29–60.

Asai, M., Konishi, Y., Oizumi, Y. & Nishika, M. 2007 Growth and breakdown of low-speed streaks leading to wall turbulence. *J. Fluid Mech.* **586**, 371–396.

Asai, M., Manigawa, M. & Nishioka, M. 2002 The instability and breakdown of near wall low-speed streaks. *J. Fluid Mech.* **455**, 289–314.

Aubertine, C. D. & Eaton, J. K. 2006 Reynolds number scaling in a non-equilibrium turbulent boundary layer with mild adverse pressure gradient. *Intl J. Heat Fluid Flow* **27**, 566–575.

Bernard, A., Foucaut, J. M., Dupont, P. & Stanislas, M. 2003 Decelerating boundary layer : a new scaling and mixing length model. *AIAA J.* **41** (2), 248–255.

Brandt, L. 2007 Numerical studies of the instability and breakdown of a boundary-layer low-speed streak. *Eur. J. Mech.* (B/Fluids) **26**, 64–82.

Brandt, L., Cossu, C., Chomaz, J.-M., Huerre, P. & Henningson, D. S. 2003 On the convectively unstable nature of optimal streaks in boundary layers. *J. Fluid Mech.* **485**, 221–242.

Brandt, L. & Henningson, D. S. 2002 Transition of streamwise streaks in zero-pressure-gradient boundary layers. *J. Fluid Mech.* **472**, 229–261.

Brandt, L. & de Lange, H. C. 2008 Streak interactions and breakdown in boundary layer flows. *Phys. Fluids* **20**, 024107.

Brandt, L., Schlatter, P. & Henningson, D. S. 2004 Transition in boundary layers subject to free-stream turbulence. *J. Fluid Mech.* **517**, 167–198.

Castillo, L. & George, W. K. 2001 Similarity analysis for turbulent boundary layers with pressure gradient: Outer flow. *AIAA J.* **39**, 41–47.

Clauser, F. H. 1954 Turbulent boundary layers in adverse pressure gradients. *J. Aero. Sci.* **21** (2), 91–108.

Cornea, N. D., Silver, D. & Min, P. 2007 Curve-skeleton properties, applications, and algorithms. *IEEE Trans. Vis. Comput. Graphics* **13** (3), 530–548.

Cossu, C., Pujals, G. & Depardon, S. 2009 Optimal transient growth and very large-scale structures in turbulent boundary layers. *J. Fluid Mech.* **619**, 79–94.

Elofsson, P. A., Kawakami, M. & Alfredsson, P. H. 1999 Experiments on the stability of streamwise streaks in plane Poiseuille flow. *Phys. Fluids* **11**, 915–930.

Gallaire, F., Marquillie, M. & Ehrenstein, U. 2007 Three-dimensional transverse instabilities in detached boundary layers. *J. Fluid Mech.* **571**, 221–233.

Gonzales, R. & Woods, R. 2008 *Digital Image Processing*, 3rd edn. Upper Saddle River, NJ: Prentice Hall.

Hall, P. & Horseman, N. J. 1991 The linear inviscid secondary instability of longitudinal vortex structures in boundary layers. *J. Fluid Mech.* **232**, 357–375.

Hoepffner, J., Brandt, L. & Henningson, D. S. 2005 Transient growth on boundary layer streaks. *J. Fluid Mech.* **537**, 91–100.

Jiménez, J. & Moin, P. 1991 The minimal flow unit in near wall turbulence. *J. Fluid Mech.* **225**, 221–240.

Jiménez, J. & Pinelli, A. 1999 The autonomous cycle of near wall turbulence. *J. Fluid Mech.* **389**, 335–359.

Kawahara, G., Jiménez, J., Uhlmann, M. & Pinelli, A. 1998 *The instability of streaks in near-wall turbulence*. Annual Research Brief, Center for Turbulence Research, p. 155.

Laval, J.-P. & Marquillie, M. 2009 Direct numerical simulations of converging–diverging channel flow. In *Progress in Wall Turbulence: Understanding and Modelling* (ed. M. Stanislas, J. Jimenez & I. Marusic, pp. 203–210, April 21–23. Springer.

Lee, J.-H. & Sung, H. J. 2008 Effects of an adverse pressure gradient on a turbulent boundary layer. *Intl J. Heat Fluid Flow* **29**, 568–578.

Lee, J.-H. & Sung, H. J. 2009 Large scale structure of turbulent boundary layer subjected to an adverse pressure gradient. In *6th International Symposium on Turbulence and Shear Flow Phenomena*, pp. 153–158. Seoul, Korea, 22–24 June, 2009.

Lin, J., Laval, J.-P., Foucaut, J.-M. & Stanislas, M. 2008 Quantitative characterization of coherent structures in the buffer layer of near-wall turbulence. Part 1: Streaks. *Exp. Fluids* **45** (6), 999–1013.

Mans, J., de Lange, H. C. & van Steenhoven, A. A. 2007 Sinous breakdown in a flat plate boundary layer exposed to free-stream turbulence. *Phys. Fluids* **19**, 088101.

Marquillie, M., Laval, J.-P. & Dolganov, R. 2008 Direct numerical simulation of separated channel flows with a smooth profile. *J. Turbulence* **9** (1), 1–23.

Na, Y. & Moin, P. 1998 Direct numerical simulation of a separated turbulent boundary layer. *J. Fluid Mech.* **374**, 379–405.

Nayar, O. & Ortega, U. 1993 Computation of selected eigenvalues of generalized eigenvalue problems. *J. Comput. Phys.* **108**, 8–14.

Palágyi, K. & Kuba, A. 1999 A parallel 3D 12-subiteration thinning algorithm. *Graph. Models Image Process.* **61**, 199–221.

Palágyi, K., Tschirren, J., Hoffman, E. A. & Sonka, M. 2006 Quantitative analysis of pulmonary airway tree structures. *Comput. Biol. Med.* **36**, 974–996.

Park, J., Hwang, Y. & Cossu, C. 2011 On the stability of large-scale streaks in turbulent Couette and Poiseuille flows. *C. R. Mécanique* **339**, 1–5.

Reddy, S. C., Schmid, P. J., Baggett, J. S. & Henningson, D. S. 1998 On the stability of streamwise streaks and transition thresholds in plane channel flow. *J. Fluid Mech.* **455**, 269–303.

Reynolds, W. C. & Hussain, A. K. M. F. 1972 The mechanics of an organized wave in turbulent shear flow. Part 3. Theoretical models and comparison with experiments. *J. Fluid Mech.* **54**, 263–288.

Schlatter, P., Brandt, L., de Lange, H. C. & Henningson, D. S. 2008 On streak breakdown in bypass transition. *Phys. Fluids* **20**, 101505.

Schmid, P. J. & Henningson, D. S. 2001 *Stability and Transition in Shear Flows*. Springer.

Schoppa, W. & Hussain, F. 2002 Coherent structure generation in near wall turbulence. *J. Fluid. Mech.* **453**, 57–108.

Schoppa, W., Hussain, F. & Metcalfe, R. W. 1995 A new mechanism of small-scale transition in a plane mixing layer: core dynamics of spanwise vortices. *J. Fluid Mech.* **298**, 23–80.

Shah, S. I., Stanislas, M. & Laval, J.-P. 2010 A specific behavior of adverse pressure gradient near wall flows. In *Progress in Wall Turbulence: Understanding and Modelling* (ed. M. Stanislas, J. Jimenez & I. Marusic), pp. 257–265., April 21-23. Springer.

Simpson, R. L. 1981 A review of some phenomena in turbulent flow separation. *Trans. ASME: J. Fluids Engng* **103**, 520–533.

Skåre, P. E. & Krogstad, P.-Å 1994 A turbulent boundary layer near separation. *J. Fluid Mech.* **272**, 319–348.

Skote, M., Haritonidis, J. H. & Henningson, D. S. 2002 Varicose instabilities in turbulent boundary layers. *Phys. Fluids* **14** (7), 2309–2323.

Skote, M. & Henningson, D. S. 2002 Direct numerical simulation of separating turbulent boundary layers. *J. Fluid Mech.* **471**, 107–136.

Song, S. & Eaton, J. K. 2004 Reynolds number effects on a turbulent boundary layer with separation, reattachment, and recovery. *Exp. Fluids* **36**, 246–258.

Spalart, P. R. & Watmuff, J. H. 1993 Experimental and numerical investigation of a turbulent boundary layer with pressure gradients. *J. Fluid Mech.* **249**, 337–371.

Waleffe, F. 1997 On a self-sustaining process in shear flows. *Phys. Fluids* **9**, 883–900.

Wilcox, D. C. 1993 *Turbulence Modeling for CFD*. DCW Industries, Inc.